

MIT Open Access Articles

Aneuploidy Causes Non-genetic Individuality

The MIT Faculty has made this article openly available. **Please share** how this access benefits you. Your story matters.

Citation: Beach, Rebecca R. et al. "Aneuploidy Causes Non-Genetic Individuality." Cell 169, 2 (April 2017): 229–242 © 2017 Elsevier Inc

As Published: <http://dx.doi.org/10.1016/J.CELL.2017.03.021>

Publisher: Elsevier BV

Persistent URL: <http://hdl.handle.net/1721.1/116147>

Version: Author's final manuscript: final author's manuscript post peer review, without publisher's formatting or copy editing

Terms of use: Creative Commons Attribution-NonCommercial-NoDerivs License





HHS Public Access

Author manuscript

Cell. Author manuscript; available in PMC 2018 April 06.

Published in final edited form as:

Cell. 2017 April 06; 169(2): 229–242.e21. doi:10.1016/j.cell.2017.03.021.

Aneuploidy causes non-genetic individuality

Rebecca R. Beach¹, Chiara Ricci-Tam², Christopher M. Brennan¹, Christine A. Moomau¹,
Pei-hsin Hsu¹, Bo Hua², Rebecca E. Silberman¹, Michael Springer², and Angelika Amon^{1,3,*}

¹David H. Koch Institute for Integrative Cancer Research, Howard Hughes Medical Institute, Massachusetts Institute of Technology, Cambridge, MA 02139, USA

²Department of Systems Biology, Harvard Medical School, Boston, MA 02115, USA

SUMMARY

Phenotypic variability is a hallmark of diseases involving chromosome gains and losses, such as Down Syndrome and cancer. Allelic variances have been thought to be the sole cause of this heterogeneity. Here, we systematically examine the consequences of gaining and losing single or multiple chromosomes to show that the aneuploid state causes non-genetic phenotypic variability. Yeast cell populations harboring the same defined aneuploidy exhibit heterogeneity in cell cycle progression and response to environmental perturbations. Variability increases with degree of aneuploidy and is partly due to gene copy number imbalances, suggesting subtle changes in gene expression impact the robustness of biological networks and cause alternate behaviors when they occur across many genes. As inbred trisomic mice also exhibit variable phenotypes, we further propose that non-genetic individuality is a universal characteristic of the aneuploid state that may contribute to variability in presentation and treatment responses of diseases caused by aneuploidy.

eTOC BLURB

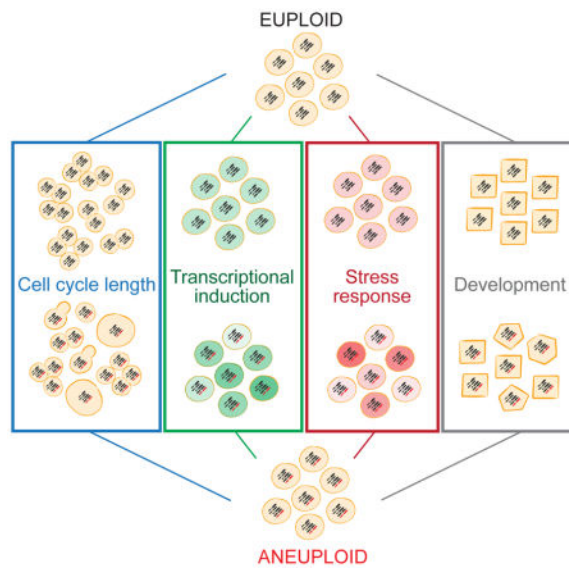
A systematic study of the consequences of gaining and losing single or multiple chromosomes shows that non-genetic phenotypic variability is a universal characteristic of the aneuploid state.

*Corresponding author: Angelika Amon, 77 Massachusetts Avenue, 76-561, Cambridge, MA 02139, Phone: (617) 258-6559, Fax: (617) 258-6558, angelika@mit.edu.

³Lead contact

AUTHOR CONTRIBUTIONS R.B., C.R., B.H., C.B., C.M., P.H., R.S., M.S. and A.A. designed the experiments. R.B., C.R., B.H., C.B., C.M., P.H. and R.S. performed experiments and analyzed results. R.B., C.R., B.H., C.B., C.M., P.H., R.S., M.S. and A.A. wrote the manuscript. All authors read and approved the final manuscript.

Publisher's Disclaimer: This is a PDF file of an unedited manuscript that has been accepted for publication. As a service to our customers we are providing this early version of the manuscript. The manuscript will undergo copyediting, typesetting, and review of the resulting proof before it is published in its final citable form. Please note that during the production process errors may be discovered which could affect the content, and all legal disclaimers that apply to the journal pertain.



Keywords

aneuploidy; non-genetic heterogeneity; cell-to-cell variability; gene dosage effects; biological noise; Down Syndrome; cancer

INTRODUCTION

Aneuploidy, a genomic state defined by whole chromosome gains and losses, is the leading cause of miscarriage and mental retardation in humans and a hallmark of cancer. A remarkable characteristic of diseases caused by unbalanced karyotypes is variability in presentation. In Down Syndrome (Trisomy 21), for example, 87.5% of fetuses die in utero, while some individuals reach age 60 or more (reviewed in Roper and Reeves, 2006). High variability is also observed in degree of facial dysmorphology, cognitive ability, hypotonia, and dermatoglyphic features at birth and in disease predisposition. This phenotypic variability has been attributed to allelic variance among individuals (reviewed in Roper and Reeves, 2006). Here we show that phenotypic variability is inherent to the aneuploid state, providing an additional potential explanation for the heterogeneity observed in diseases caused by large-scale karyotypic abnormalities.

Gains and losses of genes encoded on autosomes generally lead to corresponding changes in gene expression (reviewed in Henrichsen et al., 2009); therefore, it is not surprising that mis-segregating entire chromosomes has severe consequences. Aneuploid cells exhibit widespread aneuploidy-associated stresses including proliferation defects, elevated levels of protein aggregates, and genomic instability (reviewed in Siegel and Amon, 2012) and gene-specific phenotypes where changes in dosage of specific genes cause specific phenotypes (i.e. Sheltzer et al., 2011).

Studies of aneuploidy to date have largely been confined to cell lines with chromosome gains (Stinglele et al., 2012; Torres et al., 2007; Williams et al., 2008) because cell lines with

chromosome losses are difficult to maintain (Alvaro et al., 2006; Anders et al., 2009). Thus, it is not known how chromosome loss impacts cell physiology or whether monosomic cells exhibit the same aneuploidy-associated stresses that are widespread among cells with chromosome gains. Nor is it known how quickly aneuploidy-associated phenotypes develop following chromosome mis-segregation. Here we employ a system that allows us to examine the immediate consequences of defined chromosome gains and losses in budding yeast. Our analyses reveal that the adverse effects of aneuploidy on cell proliferation are immediate for both chromosome gains and losses. We further find high cell-to-cell variability in cell cycle progression among cells harboring the same aneuploidies. We identify gene copy number imbalances caused by the aneuploid state as one source of this variability and show that stochastic DNA damage due to gene imbalances causes high variance in S phase and early mitosis duration. Responses to environmental perturbations also vary among cells of the same aneuploid karyotype, indicating that aneuploidy impacts the robustness of multiple—perhaps all—biological processes. Finally, we find that inbred trisomic mouse embryos exhibit phenotypic variability. While subtle changes in gene dosage of individual genes have little effect on the robustness of biological networks, our results show that subtle changes in gene dosage across many genes can promote alternate behaviors.

RESULTS

A system to examine the immediate consequences of chromosome mis-segregation

In budding yeast, chromosomes that cannot attach to the mitotic spindle due to centromere failure are retained in the mother cell (Murray and Szostak, 1983). To induce chromosome mis-segregation, we replaced the endogenous centromere of each chromosome with a conditional centromere: a construct containing the galactose inducible/glucose repressible *GALI* promoter adjacent to the centromere (Hill and Bloom, 1987; Figure S1A). In the presence of galactose, transcription through the centromere prevents kinetochore formation, thus causing chromosome mis-segregation. To follow chromosome mis-segregation, we introduced an *E. coli lac* operator array near the conditional centromere and expressed a GFP-LacI fusion to visualize the array (GFP dot; Straight et al., 1996; Figure S1A). Using this system, 67–93% of mother cells retained both sister chromatids harboring the conditional centromere upon addition of galactose (Figure S1B).

In a haploid strain, chromosome mis-segregation generates nullisomes (N-1)—which are inviable—and disomes (N+1); in a diploid strain, monosomes (2N-1) and trisomes (2N+1) are generated. To ensure induction of mis-segregation of one chromosome did not lead to nondisjunction of other chromosomes, we followed the segregation of a large chromosome (IV) and a small chromosome (V) one cell division (3 hours) and 2–3 divisions (5 hours) after inducing mis-segregation of an unrelated chromosome. Inducing mis-segregation of chromosomes I, II, VIII, IX, XI or XIII did not cause chromosomes IV or V to mis-segregate (Figure S1C), indicating that inactivating one centromere does not substantially destabilize other chromosomes.

We generated a large number of strains harboring single or multiple conditional centromeres (Method Details). This enabled us to examine the consequences of mis-segregating up to 8 chromosomes and to systematically analyze the consequences of chromosome losses. We

conducted all of our cytological analyses in strains containing GFP dots on the mis-segregating chromosome(s) to ensure that we only analyzed cells that had indeed gained or lost a chromosome.

Chromosome mis-segregation leads to rapid changes in cellular protein composition

Quantitative proteomic analyses of budding yeast cells harboring an additional chromosome showed that approximately 80% of proteins encoded on the disomic chromosome are expressed according to their gene dosage (Dephoure et al., 2014; Torres et al., 2010). To determine how quickly protein levels change upon chromosome gain, we measured protein content of haploid cells that had gained a copy of chromosome IV (disome IV) immediately after chromosome mis-segregation (1 hour) and 2 cell divisions later (5 hours). As a control we measured protein content of cells constitutively harboring an additional chromosome IV (henceforth chronic disomes). Proteome quantification by TMT showed that levels of proteins encoded on the disomic chromosome were increased in chronic disome IV. However, the increase was only 1.4-fold instead of two-fold, likely due to the ‘ratio compression’ effect, a well-known artifact occurring in isobaric labeling analyses (Figure 1A; reviewed in Christoforou and Lilley, 2012). We corrected for ratio compression in our analysis.

We induced mis-segregation of chromosome IV and enriched for cells that were disomic for chromosome IV (see Method Details). The enrichment resulted in cultures containing 67% disome IV cells, 20% euploid cells, and 13% cells lacking chromosome IV (nullisomes) one hour following chromosome mis-segregation. Five hours later, the population was comprised of 61% disomes, 34% euploids, and 5% nullisomes. Based on these distributions we calculated the mean \log_2 of the relative protein abundance ratio for proteins on chromosome IV to be 0.12 at 1 hour and 0.28 at 5 hours in the extreme where proteins are only diluted by proliferation; in the other extreme where protein turnover is instantaneous, we expected values of 0.27 at 1 hour and 0.28 at 5 hours (see Method Details). Our experimental analysis revealed that proteins encoded on chromosome IV were elevated compared to proteins encoded on the euploid chromosomes 1 hour following chromosome mis-segregation, with a mean \log_2 protein abundance ratio of 0.21 for proteins on chromosome IV. Five hours following chromosome mis-segregation the value for proteins on chromosome IV was 0.32 (Figure 1B–D). These results suggest that protein composition has not fully adjusted to genome composition in disome IV cells one hour following chromosome mis-segregation, but protein composition is equivalent to that of a chronic disome within five hours of chromosome mis-segregation. We conclude that chromosome mis-segregation leads to a rapid remodeling of the proteome to reflect the cell’s genetic makeup.

Chromosome gains and losses cause defects in cell division

We next investigated how quickly cell proliferation defects arise following chromosome mis-segregation. To measure cell proliferation following chromosome mis-segregation, we first examined colony formation 40–48 hours after induction of aneuploidy, when colony size was still increasing exponentially (Figure 1E). This analysis led to two observations. First, proliferation defects in monosomes were more severe than those of disomes or trisomes (Figures 1F, S1B). Second, colony size was inversely correlated with degree of

aneuploidy (Figure 1F). The observation that the negative fitness slope of trisomes is less steep than that of disomes further suggests that it is the relative ratio of aneuploid to euploid gene dosage that is mainly responsible for the observed fitness defects. Doubling gene dosage relative to base ploidy of the cell, as in disomes, is proportionally more detrimental than increasing gene dosage by 50% relative to base ploidy, as in trisomes. We conclude that: 1) both chromosome gain and loss impair cellular fitness; 2) changes in relative expression levels of genes are responsible for the fitness defects observed in cells with chromosome gains; and 3) the fitness defect of monosomes is likely a composite of aneuploidy-associated stresses and haploinsufficiency.

Effects of chromosome loss on cell cycle progression

To more carefully define the cell cycle defects caused by chromosome loss, we analyzed cell cycle progression following chromosome loss by time-lapse microscopy. We used mCherry-Cdc3 and Spc42-dsRed or Spc42-GFP fusion proteins along with GFP dots on the mis-segregating chromosome(s) to follow cell cycle progression. Cdc3 is a component of the septin ring that forms at the site of bud formation from the time of entry into the cell cycle until exit from mitosis (Kim et al., 1991). Thus, the time during which a cell lacks a Cdc3 ring estimates the time a cell spends in G1. Spc42 is a component of the spindle pole body (SPB; Donaldson and Kilmartin, 1996). The distance between SPBs and the separation of sister chromatids as analyzed by GFP dot separation indicate anaphase onset.

Doubling time measurements revealed reduced cell proliferation in all monosomic strains analyzed (Figure 2A). This analysis agreed with our colony size measurements but was not perfectly correlated (i.e. monosomes XII and XIV) because doubling time measurements do not account for cells that stop dividing, which occurs frequently in some monosomic strains. We further observed that the cell cycle delay and frequency of cell cycle arrest increased with degree of monosomy (Figure 2A). Strains with the highest degree of monosomy appeared to have less of a cell cycle delay than strains with lower levels of monosomy; however, this is because cells that stop dividing—a frequent occurrence in complex monosomes (Figure 2A, grey points; Figure S2A)—cannot be included in the doubling time measurements and thus cell proliferation defects are underreported.

In-depth cell cycle analyses revealed that 14 of 15 monosomes exhibited G1 delays that increased with degree of monosomy ($r^2 = 0.89$; Figure S2B,E). Delays in other cell cycle stages were also common (Figure S2C,D). We conclude that loss of most chromosomes impacts multiple cell cycle stages.

Our live-cell analyses also revealed that monosomic cells of the same karyotype exhibited dramatic cell-to-cell variability in cell cycle duration (Figures 2A–E; S2B–D; Table S1). To quantify heterogeneity, we calculated the standard deviation of G1 duration and of the time it took cells to complete S phase and early mitosis (bud emergence to anaphase onset, henceforth S+early M phase) and found high variability in both cell cycle periods (Figures 2B–E; S2B,C). Furthermore, variability in G1 duration increased with degree of monosomy (Figure 2B). S+early M phase duration variability appeared less correlated with degree of monosomy, but this appearance may be misleading as cells with multiple monosomies only undergo 1–2 cell divisions before arresting in G1 (Figure S2A). Variability in the first and

second divisions following chromosome mis-segregation may be smaller than it would be in later divisions (if complex monosomes continued to divide) because levels of long-lived proteins may not yet have adjusted to the monosomic state and thus have not yet become limiting.

To determine whether variability was driven by a small number of extremely slowly dividing cells or if it reflected a wide spread of proliferation rates, we asked how many of the slowest dividing cells had to be eliminated from monosomic cell populations for variance of the monosome population to resemble that of euploid cells (Figure 2F). In 6 of 10 monosomes analyzed, increased variability in S+early M duration was driven by a few cells with extreme cell cycle delays (Figure 2F). In the remaining monosomes, a higher fraction of the population (~20%) conferred increased heterogeneity in S+early M. About 10–30% of the population caused increased G1 duration variability in most monosomes (Figure 2F). We conclude that monosomy interferes with multiple aspects of cell proliferation and that the degree of the defect varies greatly among cells of the same karyotype.

Cells harboring additional chromosomes exhibit heterogeneity in cell cycle kinetics

Next we examined cell-to-cell variability in cell cycle duration following chromosome gain(s) in haploid cells. Consistent with previous results, cell division rates were decreased in all disomes, with most disomes exhibiting delays in both G1 and S+early M phase (Figures 3A, S3A–C). Interestingly, disomes—like monosomes—exhibited significant cell-to-cell variability in G1 and S+early M phase lengths that increased with degree of disomy (Figures 3B,C; S3D; Table S1). In the majority of strains with single chromosome gains, variability in G1 and S+early M phase length was driven by 20% of the population or less; however, variability was due to a wide spread of G1 and S+early M lengths in strains harboring multiple disomies (Figure 3D).

Most aneuploidy-associated phenotypes are attenuated when base ploidy is increased—that is, they are more severe in disomes than in trisomes (Torres et al., 2007). To some extent, increased ploidy buffered cell cycle duration heterogeneity (Figures 3; S3). Variability in total cell cycle length and S+early M phase duration was partially attenuated by increased ploidy (Figure 3I–K). Our data demonstrate that increased cell-to-cell variability in cell cycle progression is a universal feature of the aneuploid state in yeast. Our data further indicate that this heterogeneity is caused in part by the amount of overproduced protein with respect to base ploidy and implicate overexpressed proteins or proteins that are not correctly assembled into their biological complexes as contributing to non-genetic variability in aneuploid cells.

Cell division length variability is stochastic

What are the origins of cell-to-cell variability in cell cycle duration in aneuploid cells? Although aneuploid cells are genomically unstable (Blank et al., 2015; Nicholson et al., 2015; Passerini et al., 2016; Sheltzer et al., 2011; Zhu et al., 2012), mutation-induced population heterogeneity is an unlikely cause. The system we employ examines the immediate effects of mis-segregating a specific chromosome, precluding the accumulation of suppressor mutations. Nevertheless, to exclude the possibility that heterogeneity is due to

genetic or perhaps epigenetic changes, we examined whether cell cycle timing was consistent from one division to the next. We measured division times of individual cells during two consecutive cell divisions following chromosome mis-segregation. This analysis revealed that a slow division was not predictive of a subsequent slow division, as single-cell division times for two consecutive divisions were not correlated ($r^2 = 0.019$; Figure S4A–E). We conclude that neither genetic nor epigenetic changes cause population heterogeneity in aneuploid cells.

Stochastic DNA damage contributes to population heterogeneity in aneuploid strains

If genetic and epigenetic alterations are not responsible for cell-to-cell variability, stochastic events must be the source of heterogeneity. To test this idea we first asked whether stochastic DNA damage could explain aspects of the observed cell-to-cell variability, as a previous study showed that yeast strains harboring chronic disomies experience increased DNA damage (Blank et al., 2015). We deleted *RAD9*, a gene encoding a component of the DNA damage checkpoint pathway that delays cell cycle progression in response to DNA damage (Figure 4; Table S1). *RAD9* deletion decreased cell-to-cell variability in S+early M phase duration in euploid cells (Figure 4G). This is not surprising as even euploid cells experience DNA damage, especially during live-cell imaging. The effect of deleting *RAD9* was dramatic in disomes and monosomes: cell-to-cell variability in S+early M duration decreased in all strains except monosome XI (Figure 4F). *RAD9* deletion only caused a minor decrease in G1 length variability in some aneuploid strains (Figure 4D), which is not surprising as DNA damage is predominantly repaired in S phase and G2 in yeast (Weinert and Hartwell, 1988). We conclude that stochastic DNA damage is largely responsible for variability in S+early M phase length in all but one aneuploid strain analyzed.

Deletion of *RAD9* not only decreased variability in S+early M phase length but also slightly decreased mean S+early M duration in some aneuploid strains (Figure 4C). To determine whether accelerating cell proliferation *per se* led to a decrease in cell-to-cell variability, we examined the consequences of deleting *UBP6* on cell cycle length heterogeneity. Deletion of *UBP6* attenuates levels of proteins whose abundances change most in disomic yeast strains and increases proliferative potential of most chronic disomes at 37°C and of three disomes (V, VIII, and XI) at 25°C (Dephoure et al., 2014; Torres et al., 2010). *UBP6* deletion decreased mean G1 length immediately following mis-segregation of chromosomes V, VIII and XI but did not affect cell cycle length variability (Figure S4F–L; Table S1). Our results indicate that increased variability in cell cycle length in disomic yeast strains is not solely a consequence of increased cell cycle length. As deletion of *UBP6* attenuates levels of proteins most mis-regulated in disomes yet does not affect variability, we further conclude that the most extremely deregulated genes in disomes do not cause cell cycle length variability.

G1 length variability is attenuated in strains harboring chronic disomies

Heterogeneity in cell cycle duration immediately following chromosome mis-segregation was dramatic, ranging from near euploid division times in some cells to cell cycle arrest in others. Is heterogeneity maintained as cells continue to divide with an unbalanced karyotype? To address this question we measured cell cycle duration in chronic disomes.

Disomy of chromosome I, VIII, XIV or XVI causes significant variability in G1 and S+early M phase duration immediately following chromosome mis-segregation (“Acute Dis”; Figure 5). Chronic disomes I, VIII, XIV and XVI also exhibited cell-to-cell variability that—like in acute disomes—was of non-genetic origin as single-cell division times for two consecutive divisions were generally not significantly correlated (Figure S5). However, variability in G1 duration was attenuated in 3 of 4 chronic disome strains compared to acute disomes (Figure 5; Table S1). Variability in S+early M phase was only attenuated in chronic disome I. We conclude that cell-to-cell variability in G1 duration is initially high following chromosome mis-segregation but attenuates upon continuous selection for an aneuploid karyotype.

Aneuploidy increases variability in the response to environmental perturbations

Next we determined whether aneuploidy increases cell-to-cell variability in other biological processes. We analyzed the response of disomes I, II, VIII, IX, XI, XIII, and XVI to three perturbations: galactose, DTT, and heat shock. Strains were analyzed at single-cell resolution by flow cytometry with fluorescent reporter fusions that respond to each perturbation (Method Details; Figure 6), as gene expression is a classic model in the study of population heterogeneity (Raser and O’Shea, 2005). Additionally, disomes V, X, XII, and XIV were analyzed in a subset of the three environments (Figure S6). Strains with *GAL1pr-YFP* were grown in medium containing 0.25% galactose with no other sugars—a maximally inducing condition (Figure 6A–B). Strains with heat shock element (HSE) motifs ($P_{4xHSE-YFP}$) controlled by the transcription factor Hsf1 were grown at 39°C (a temperature where most euploid cells robustly respond to heat-shock with minimal cell death; Figures 6C–D and S6A–B). Strains with a promoter containing four unfolded protein response element (UPRE) motifs ($P_{4xUPRE-GFP}$) regulated by Hac1 were grown in medium containing 0.625mM DTT, a concentration where cells robustly respond (Figures 6E–F and S6C–D). While the mean significantly varied in 19 of 26 strain condition pairings (p-values < 0.05 by Wilcoxon rank sum test; Figures 6A,C,E and S6A,C) there was no pattern to whether the mean increased or decreased (Table S2). However, the standard deviation increased in all 18 experimental-condition pairs where variation in standard deviation was observed (p-values < 0.05 by Wilcoxon rank sum test; Figures 6B,D,F and S6B,D and Table S2). The fold increases in standard deviation varied from 1.03 to 1.5-fold. In total, our results indicate that aneuploidy increases cell-to-cell variability in a number of different biological responses.

In addition to variations in the maximal response, variations can also exist in the kinetics of response to a signal and the concentration at which cells respond. Therefore, we titrated glucose to measure the concentration of glucose at which cells repress the *GAL1pr-YFP* reporter construct in medium that contains 0.25% galactose (Figure S7). All disomes tested were more sensitive to glucose inhibition (p-values < 0.05 by Wilcoxon rank sum test; Figure S7B). In addition, we measured the time to induce *GAL1pr-YFP* following shift from raffinose to galactose (time = 0 in Figure S7C–D). All disomic populations except disome I harbored a substantial fraction of cells that were delayed in *GAL1pr-YFP* induction compared to euploid populations (Figure S7C–D). The time for all cells to completely induce the GAL response also varied among the disomes, in some cases increasing and in others decreasing. Together, these results support that the vast majority of disomes are more variable in their response to galactose.

The increase in standard deviation of the response could result from pathway specific increases in variation (intrinsic) or global increases in variation (extrinsic). Because we had measured a number of disomic strains under multiple conditions we were able to ask whether an increase in variation in response to one stimulus was correlated with an increase in variation in a second stimulus. The results suggest both extrinsic and intrinsic components. The extrinsic component is supported by several strains having higher standard deviations in all conditions (Figure 6B,D,F; significance of 0.06 by Wilcoxon rank sum test). The intrinsic component is supported by strains such as disome VIII that had increased variation in two conditions but not in a third (Figure 6B,D,F).

To alternately assess the degree of intrinsic versus extrinsic noise, we measured the correlation in expression of two promoters (*GAL1pr-YFP* and *TDH3pr-mCherry*) at a single cell level in five disomic strains (Figure 6G). After binning for cell size (Method Details), two of the strains had an increased correlation compared to euploid cells while three of the strains had a decreased correlation (p-values < 0.05 by Wilcoxon rank sum test). Our data show that increased variability in the response of aneuploid cells to multiple environmental stimuli is caused by both intrinsic and extrinsic sources of variation.

Aneuploidy increases phenotypic variability in mammals

Is increased population heterogeneity a unique feature of aneuploid budding yeast or a more general property of the aneuploid state? To address this question we examined the effects of chromosome gain on phenotypic variability in inbred mouse strains. We used Robertsonian translocations backcrossed at least 10 times into the C57BL/J6 background to generate isogenic euploid, trisomy 13, and trisomy 19 embryos (Williams et al., 2008). In crosses involving Robertsonian translocations, litter size is usually small and trisomic embryos represent less than 16% of offspring (Pfau and Amon, 2015), severely limiting the number of animals we were able to analyze. Nevertheless, it was evident that phenotypic variability was high among trisomy 19 embryos compared to isogenic euploid littermate controls. We observed variability in facial morphology, degree of nuchal edema and hemorrhaging at embryonic day 15.5 (Figure 7A). To quantify variability we measured the maximal width of nuchal translucency, a classic prenatal test to assess degree of nuchal edema, which is an indicator of chromosomal abnormalities in human pregnancies. Variability in nuchal edema thickness was significantly higher in trisomy 19 embryos than in euploid embryos (p<0.05 by permutation analysis and p<0.005 by F-test on the variance; Figure 7B). Variability in morphology was also observed among trisomy 13 embryos despite only obtaining one litter with trisomy 13 embryos (Figure 7C). We conclude that aneuploidy causes phenotypic variability in inbred trisomy 19 embryos and likely also in trisomy 13 embryos.

DISCUSSION

Phenotypic differences in genetically identical populations have been observed in a variety of experimental settings (Cerulus et al., 2016; reviewed in Raj and van Oudenaarden, 2008; Raser and O'Shea, 2005). Variability can arise from stochastic synthesis and degradation of molecules (Elowitz et al., 2002; Paulsson, 2004) as well as binomial partitioning at cell division (Huh and Paulsson, 2011). Fluctuations are exacerbated when molecules are at low

copy number or are segregated as a unit (Jajoo et al., 2016; Uphoff et al., 2016). Mechanisms have been described that counteract these fluctuations to make biological processes robust (reviewed in Arias and Hayward, 2006), but regulatory networks can exhibit alternate behaviors when buffering mechanisms are perturbed (Mileyko et al., 2008). We show here that chromosome-scale changes in gene dosage severely impact the robustness of every biological network analyzed. Robustness decreases with degree of aneuploidy, indicating that while subtle changes in gene dosage of individual genes have little effect on the robustness of biological networks, gene dosage changes across many genes can promote alternate behaviors. We propose that this universal characteristic of the aneuploid state may help explain the variability in presentation and treatment responses of diseases caused by karyotypic abnormalities.

Aneuploidy decreases robustness of biological networks

Recent work has shown that karyotypically heterogeneous populations of aneuploid *S. cerevisiae* and *C. albicans* exhibit a wide range of phenotypes, particularly under stress, which can be beneficial in adaptation to different environments (Chen et al., 2015; Hickman et al., 2015). We report here that *karyotypically homogeneous* populations of aneuploid cells exhibit increased phenotypic variation as compared to euploid cells. All chromosome gains and losses analyzed cause a dramatic increase in variance in G1 and/or S+early M phase duration, with increases in both cell cycle stages for many aneuploidies. Two lines of evidence indicate that this variability is not due to genetic heterogeneity. First, the inducible system to generate aneuploid cells employs strains that are propagated in the euploid state and acutely induced to mis-segregate specific chromosomes, which avoids accumulation of genetic alterations selected for by an aneuploid karyotype. Second, cell cycle delays observed in an individual cell are not consistent from one division to the next, indicating that delays are caused by stochastic and not heritable events.

Heterogeneity in cell cycle duration was also observed in strains with chronic aneuploidies, and cell cycle delays were not heritable, arguing for non-genetic rather than genetic heterogeneity. Furthermore, chronic aneuploid strains are variable for several cellular responses in addition to cell cycle timing. Population variation in gene expression increased in multiple aneuploid strains in response to an alternate carbon source and in response to two different cellular stresses: heat shock and DTT. Increased variability occurred across all tested conditions that led to a response in our reporters. Together, these results lead to the unanticipated conclusion that aneuploidy causes an increase in non-genetic variability in many different cellular responses. In fact, unaffected pathways may be in the minority.

Origins of non-genetic individuality

How does aneuploidy increase cellular variability? Previous studies suggested that deterministic processes are responsible for cell-to-cell variability in cell cycle progression in euploid cells (Sandler et al., 2015). Our analyses indicate that stochastic DNA damage, leading to activation of the DNA damage checkpoint pathway, is a significant source of heterogeneity in S+early M duration. The subtle S phase defects and genomic instability that aneuploid cells experience (Blank et al., 2015; Sheltzer et al., 2011; Zhu et al., 2012) are

likely the cause for activation of the DNA damage checkpoint pathway in a fraction of aneuploid cells.

In contrast to variability in S+early M duration, DNA damage was not responsible for G1 length heterogeneity in most aneuploid strains. Additional factors that contribute to variability in G1 remain unknown. However, it is of note that most stress response pathways delay cells in G1 (Herrero et al., 2003) and cellular stresses have been shown to increase phenotypic variability under some conditions (Axelrod et al., 2015). Various stresses associated with the aneuploid state, such as protein folding, metabolic and oxidative stress, may contribute to G1 length variability in aneuploid strains. We further note that many aneuploidies interfere with macromolecule biosynthesis, which controls G1 length (Thorburn et al., 2013). Thus, cell-to-cell variability in biosynthetic rates may also contribute to G1 length variability in aneuploid strains.

We also do not yet know how aneuploidy causes heterogeneity in gene expression. Gene dosage changes may alter expression—for instance, disome XIII may affect the response to galactose by changing the dosage of the Gal80 repressor encoded on chromosome XIII—yet it is unclear how dosage changes would increase population variability. Instead, increased variability in gene expression may be caused by an indirect source such as cellular stress, which is a universal feature of the aneuploid state. Previous studies showed that environmental stresses decrease growth rate, which can lead to decreased expression of some transcription factors, thus increasing their variability and thereby the variability of the responses they control (Kashiwagi et al., 2006). As aneuploidy causes a variety of cellular stresses, this alone is likely to be a key contributor to the observed increased cell-to-cell variability. Also, multiple lines of evidence indicate that phenotypic heterogeneity allows populations to bet-hedge under stressful situations, which decreases the mean fitness of the population but increases the geometric mean of the population, thereby allowing cells to survive in extreme situations (Acar et al., 2008; Beaumont et al., 2009; Fridman et al., 2014; Levy et al., 2012). Increased variability in aneuploid cells could also be related to this phenomenon.

Ultimately, general features of the aneuploid state are likely to be the source of population heterogeneity. Many aneuploid yeast strains have decreased protein synthesis rates (Thorburn et al., 2013) which may lead to decreased production of rare proteins. Unequal partitioning of such rare proteins could cause phenotypic variability. Changes in relative ratios of gene products also contribute to cell-to-cell variability. Higher base ploidy partially buffers aneuploidy-induced cell-to-cell variability at least in S+early M phase duration. We do not yet know which genes decrease robustness upon doubling or halving gene dosage. Few genes in yeast cause substantive cell cycle defects when dosage increases by a single extra copy (Bonney et al., 2015) and haploinsufficiency is equally rare (Deutschbauer, 2005). However, subtle changes in the dosages of network nodes such as transcription factors or regulatory enzymes (i.e. protein kinases) may have widespread effects on the activities of the biological pathways that they control (Mileyko et al., 2008; Rancati et al., 2008), making cells more susceptible to intracellular and extracellular noise.

Implications for cell-to-cell variability in euploid populations

Fluctuations in mRNA synthesis, protein synthesis and degradation, and unequal segregation of proteins have all been implicated in producing cells with alternate fates in populations of genetically identical cells (Blake et al., 2003; Elowitz et al., 2002; Huh and Paulsson, 2011; Sigal et al., 2006). Our analyses of aneuploid cells are consistent with variability in these processes being sources of biological noise. Furthermore, our data lead to the remarkable conclusion that subtle changes in gene expression (50% increases or decreases) can cause significant cell-to-cell variability when they occur at a chromosome-wide scale, especially when multiple chromosomes are involved. In contrast, changing dosage of single genes by 50% usually has little effect on the robustness of biological networks. In other words, simultaneously changing multiple nodes of a biological network in subtle ways can make the behavior of a pathway unpredictable. We propose that simultaneous subtle fluctuations in the levels and activities of network components could contribute to heterogeneity observed in euploid cells.

Implications for disease presentation and treatment

Phenotypic variability is not confined to aneuploid yeast strains. Trisomic embryos also exhibit variability in morphology. From this observation, we propose that non-genetic heterogeneity may contribute to phenotypic variability seen in constitutional aneuploidies in humans and, of course, in cancer. Comparing phenotypic variability between inbred and outbred aneuploid yeast strains may provide an opportunity to assess the degree of variability conferred by the aneuploid state itself versus allelic variation in the population.

Non-genetic heterogeneity may also explain why aneuploidy occurs frequently in experimental evolution. Increased variance has the potential to enhance population fitness in euploid populations (Cerulus et al., 2016); therefore, aneuploidy may occur in evolution as a mechanism to further increase population variance, and thus fitness.

In closing, we note that aneuploidy-associated non-genetic variability has profound implications for aneuploidy as a therapeutic target in cancer and fungal infections. Non-genetic heterogeneity may make it difficult for therapies to target specific aneuploidies. In summary, our results indicate that decreased robustness of many, if not all, biological processes is a general feature of the aneuploid state. It will be interesting to determine how increased variability in single cell behavior leads to increased variability of multicellular processes.

STAR METHODS

CONTACT FOR REAGENT AND RESOURCE SHARING

Further information and requests for resources and reagents should be directed to and will be fulfilled by the Lead Contact, Angelika Amon (angelika@mit.edu).

EXPERIMENTAL MODEL AND SUBJECT DETAILS

Yeast strains and growth conditions—All *S. cerevisiae* strains used in this study are listed in Table S3. Yeast strains were generated and manipulated as described previously

(Guthrie and Fink, 1991). Cells were grown at 30°C in YEP supplemented with 2% raffinose (YEP-R), 2% raffinose + 2% galactose (YEP-RG), or 2% glucose (YEP-D). For live-cell imaging, cells were grown in synthetic complete medium at 25°C supplemented with 2% raffinose (SC-R), 2% raffinose + 2% galactose (SC-RG), or 2% glucose (SC-D).

Yeast strains used in Figures 1–6 were as follows: Figure 1:

(A) Haploid wild-type (A38452), chronic disome IV (A24367)

(C,D) Haploid wild-type (A38452), disome IV (A38455)

(E–F) Haploid wild-type (A2587), diploid wild-type (A16629); disomes I (A38370), II (A38372), III (A38374), IV (A38376), V (A38378), VI (A38380), VII (A38382), VIII (A38384), IX (A38386), X (A38388), XI (A38390), XII (A38392), XIII (A38394), XIV (A38396), and XVI (A38398); trisomes and monosomes I (A38401), II (A38402), III (A38403), IV (A38404), V (A38405), VI (A38406), VII (A38407), VIII (A38408), IX (A38409), X (A38410), XI (A38411), XII (A38412), XIII (A38413), XIV (A38414), and XVI (A38415). Trisomes and monosomes I+II (A38753), V+X (A38755), II+V+X (A38756), I+V+X (A38758), and I+II+X (A38759) were used in this assay with a different wild-type strain (A38751).

Figure 2:

Diploid wild-type (A38656); monosomes I (A38661), II (A38663), IV (A38665), V (A38667), VIII (A38669), X (A38671), XI (A38673), XII (A38675), XIV (A38679), XVI (A38681) V+X (A38695), IV+V+VIII (A38689), II+IV+XIV (A38687), IV+V+VIII+XIV (A38691), and II+IV+V+VIII+X+XIV (A38690). The diploid wild-type strain (A38656) is marked with Spc42-GFP and mCherry-Cdc3.

Figure 3:

Haploid wild-type (A38654); disomes I (A38660), II (A38662), IV (A38664), V (A38666), VIII (A38668), X (A38670), XI (A38672), XII (A38674), XIII (A38676), XIV (A38678), XVI (A38680), V+X (A38694), II+V+X (A38682), II+X+XIV (A38684), IV+V+VIII (A38688), and II+IV+XIV (A38686); diploid wild-type (A38656); trisomes I (A38661), II (A38663), IV (A38665), V (A38667), X (A38671), XI (A38673), XII (A38675), XIV (A38679), and V+X (A38695). The haploid (A38654) and diploid (A38656) wild-type strains are marked with Spc42-GFP and mCherry-Cdc3.

Figure 4:

Strains used in this assay: haploid *RAD9* wild-type (A38654) with *RAD9* disomes I (A38660), II (A38662), V (A38666), VIII (A38668), XI (A38672), XIII (A38676); haploid *rad9* wild-type (A38770) with *rad9* disomes II (A39305), V (A38772), VIII (A39306); haploid *rad9* wild-type (A38771) with *rad9* disomes I (A39304), XI (A38773), XIII (A39307); diploid *RAD9* wild-type (A38656) with *RAD9* monosomes I (A38661), II (A38663), V (A38667), VIII (A38669), XI (A38673); diploid *rad9* wild-type (A39326) with *rad9* monosomes I (A39309), II (A39310), V (A39311), VIII (A39312), XI (A39313).

Figure 5:

Haploid wild-type (A38654) with acute disomes I (A38660), VIII (A38668), XIV (A38678), XVI (A38680); haploid wild-type (A38699) with chronic disomes I (A38701), VIII (A38702), XIV (A38704), XVI (A39285).

Figure 6:

(A–B) Wild-type (A38340); disomes I (A38341), II (A38342), VIII (A38343), IX (A38344), XI (A38345), XIII (A38346), and XVI (A39284).

(C–D) Wild-type (A38735); disomes I (A38736), II (A39280), VIII (A38738), IX (A38739), XI (A39282), XIII (A39283), and XVI (A38740).

(E–F) Wild-type (A38728); disomes I (A39275), II (A39276), VIII (A38730), IX (A39277), XI (A39278), XIII (A39279), and XVI (A38734).

(G) Wild-type (A39298); disomes I (A39299), II (A39300), IX (A39301) XI (A39302), and XVI (A39303).

Mouse strains—Trisomic mouse embryos were generated by crossing C57BL/6J mice with congenic mice heterozygous for two Robertsonian chromosomes (Williams et al., 2008). The following Robertsonian fusion chromosomes were used for these crosses: B6.Cg-Rb(11.13)4Bnr/JAmonJ, B6.Cg-Rb(13.16)1Mpl/JAmonJ, B6.CgRb(5.19)1Wh/JAmonJ, and B6Ei.Cg-Rb(9.19)163H/J.

All animal studies and procedures were approved by the Committee on Animal Care (CAC), Division of Comparative Medicine (DCM) at the Massachusetts Institute of Technology (protocol number: 0715-073-18, *In vivo* and *in vitro* characterization of aneuploid cells), and all experiments were conducted in accordance with DCM regulatory standards.

All C57BL/6J mice and congenic wild-type mice carrying Robertsonian chromosomes were healthy and immunocompetent. Husbandry and housing conditions of experimental animals were in accordance with DCM guidelines and DCM Lab Animal User's Handbook; in addition, the animals were monitored daily by the Amon lab as well as by DCM veterinarians and staff. Sample size estimation was not performed computationally; as trisomic embryos are very difficult to obtain, we sought to analyze as many trisomic embryos as was technically feasible. Animals were allocated to experimental groups based on genotype (euploid or trisomic).

METHOD DETAILS

Construction of conditional centromere strains—Strains with conditional centromeres were constructed using a PCR-based method (Anders et al., 2009; Longtine et al., 1998). Briefly, the conditional centromere construct was amplified from plasmid p1888 (see Table S5) using primers designed to target the conditional centromere construct to a particular chromosome (see Table S4). Strain A2587 was transformed with the conditional centromere constructs as previously described (Longtine et al., 1998). We replaced the

endogenous centromere with the conditional centromere construct for every single chromosome (I-XVI). With the exception of cells with a conditional centromere on chromosome XV, all strains containing the conditional centromere construct exhibited doubling times equal to that of wild-type cells when grown in medium containing glucose (data not shown). We also generated strains containing multiple conditional centromeres. This allowed us to examine the consequences of mis-segregating multiple (up to 8) chromosomes. Importantly, this system also enabled us to systematically analyze the consequences of chromosome losses on yeast cell physiology.

CEN-LacO plasmid construction: To follow chromosome mis-segregation, we introduced a *lac* operator (*E. coli*, *lacO*) array near the centromere of the chromosome containing the conditional centromere (Figure S1A). When a GFP-LacI fusion protein is expressed in these cells, it binds to the *lacO* sequences and forms a GFP dot at the *lacO* array that is visible by fluorescence microscopy (Straight et al., 1996).

Plasmids targeting the LacO array to various chromosomes (CEN-LacO plasmids; Table S5) were constructed by cloning a homology region to the specific target site with XhoI restriction sites into the SalI cut plasmid p1499 (pCM40). Plasmids were integrated at the target site by restriction enzyme digest using the enzymes listed in Table S5. Transformants were screened for gain of nourseothricin resistance (100 µg/ml). All plasmids containing the LacO array were propagated in Max Efficiency Stb12 competent cells (Invitrogen) due to the high propensity of the LacO array to recombine. All enzymes used for cloning were obtained from New England BioLabs.

HYGRO-LacO plasmid construction: A plasmid targeting the LacO array to the *hph* hygromycin B resistance gene (HYGRO-LacO; Table S5) was constructed in the same way as the Cen-LacO plasmids, using homology to the *hph* hygromycin B resistance gene. Integration of the HYGRO-LacO plasmid used a two-step process. First, the *hph* hygromycin B resistance gene was integrated into the desired site in the genome using a PCR-based method (Longtine et al., 1998). Second, the HYGRO-LacO plasmid was integrated at the *hph* site by EagI digest. Transformants were screened for loss of hygromycin resistance and gain of nourseothricin resistance.

GFP dot strain construction: Strains containing the LacO array were crossed to a strain containing the GFP-LacI fusion protein. To integrate the GFP-LacI construct into the genome, plasmid p1801 (Table S5) was linearized with NheI and transformed into A2587 cells as previously described (Guthrie and Fink, 1991).

Additional constructs: *Spc42-dsRed* and *Spc42-GFP* were constructed by PCR-based methods (Longtine et al., 1998). *mCherry-Cdc3* was constructed using the *YIp211-CDC3-mCherry* integrating plasmid (Fang et al., 2010). The *GAL1pr-YFP* reporter was integrated at the *HO* locus (Escalante-Chong et al., 2015). The *P_{4xHSE}-YFP* and *P_{4xUPRE}-GFP* reporters were constructed from single-integrating plasmids (Damon et al., 2015). To make the dual YFP-mCherry reporter for the assays described in Figure 6G, a constitutively-expressed *TDH3pr-mCherry* construct was integrated in tandem with the *GAL1pr-YFP* reporter at the *HO* locus.

Mis-segregation frequency of non-targeted chromosomes—After mis-segregation in SC-RG, cultures were released into SC-D and fixed with 3.7% formaldehyde after 3 and 5 hours of growth at room temperature. The number of GFP dots per cell was counted for 100 unbudded cells at each time point. Unbudded cells containing 2 GFP dots were classified as having mis-segregated the GFP marked chromosome. One experimental replicate was performed.

Fluorescence microscopy—For GFP dot imaging, cells were either imaged live or fixed in 3.7% formaldehyde for 15 minutes at room temperature and then resuspended in 0.1 M potassium phosphate (KPi pH 6.4)/1.2 M sorbitol. To visualize biotin labeling, cells were fixed in 3.7% formaldehyde for 15 minutes at room temperature and then resuspended in 0.1 M potassium phosphate (KPi pH 6.4)/1.2 M sorbitol with 1 µg/ml streptavidin conjugated to Alexa 568 fluorophore (Molecular Probes). Cells were then washed once in 0.1 M potassium phosphate (KPi pH 6.4)/1.2 M sorbitol. Cells were imaged using a Zeiss Axioplan 2 microscope (Carl Zeiss) and a Hamamatsu OCRA-ER digital camera (Hamamatsu).

Biotin labeling and sorting—Cells were arrested with α -factor in YEP-R medium at 30°C and labeled with biotin as described below (Smeal et al., 1996). Upon release from the G1 arrest, cells were switched to medium containing galactose (YEP-RG) to inactivate *CEN4*. Cells were then transferred to YEP-D medium at 30°C to stop further chromosome mis-segregation and grown for 1 or 5 hours. To purify populations of disomic cells for proteomic quantification following chromosome mis-segregation, we used a previously described method to purify mother cells (Smeal et al., 1996).

Cells were grown to mid-log phase in YEP-R and then arrested in G1 with the yeast mating pheromone α -factor (5 µg/ml). Following G1 arrest, cells were washed 3 times in phosphate buffered saline (PBS) pH 8.0 and labeled with EZ-Link Sulfo-NHS-LC-Biotin (1 mg biotin in PBS pH 8.0 per 1 OD₆₀₀ unit of cells; Thermo Scientific) at 4°C for 30 minutes. Biotin forms permanent amide bonds with primary amines on cell surface proteins, thus labeling the cell wall of the G1 arrested cells. As the cell wall is built *de novo* during budding, release from the G1 block in the absence of biotin results in the mother cell being labeled with biotin while the bud is not labeled. Following biotin labeling, cells were washed 4 times with PBS pH 8.0/100 mM glycine to remove excess biotin.

After biotin labeling, cells were transferred into YEP-RG medium to induce chromosome mis-segregation. Cells were grown for 120 minutes in YEP-RG at 30°C (one cell division). After nearly all cells had finished dividing, cells were transferred to YEP-D and grown at 30°C for 1 hour. To purify biotin labeled cells, cells were first washed with PBS pH 7.4/0.5% bovine serum albumin (BSA) and then incubated with anti-biotin magnetic beads (Miltenyi Biotec) in PBS pH 7.4/0.5% BSA for 15 minutes at 4°C. Cells were washed once more with PBS pH 7.4/0.5% BSA and then resuspended in PBS pH 7.4/0.5% BSA and run over LS columns fit with a pre-separation filter on a QuadroMACS separator attached to a MACS MultiStand (Miltenyi Biotec) to retain biotin-labeled cells. Biotin labeled cells were eluted from the columns with PBS pH 7.4/0.5% BSA following removal from the QuadroMACS separator. Cells were then washed once with PBS pH 7.4 and resuspended in YEP-D and grown at 30°C. Samples for analysis were taken at times indicated in Figure 1B.

Chronic disome IV cells shown in Figure 1A were grown to mid-log phase in YEP-D at 30°C and then harvested for preparation of protein extracts.

Protein quantification by mass spectrometry—Preparation of protein extracts was adapted from Dephoure et al. (2014). Briefly, cells were lysed using a FastPrep-24 (MP Biomedicals) in a buffer containing 8 M urea, 75 mM NaCl, and 50 mM Tris-Cl pH 8.2 using 3–6 cycles of 45 s at 4°C separated by 5 minute incubations at 4°C. Samples were broken until ~70% of cells had lysed as confirmed by light microscopy. Lysates were cleared by centrifugation at 14,000xg for 15 minutes at 4°C. Protein concentrations were determined using the Bradford protein assay (Bio-Rad). Further sample preparation, TMT labeling, and sample fractionation was performed as described in Dephoure et al. (2014). One biological replicate was performed. Samples were run with 3 technical replicates on a Thermo Q Exactive mass spectrometer (Thermo Fisher Scientific). Database searching was conducted using Mascot (Matrix Science).

Protein ratios were normalized to account for minor variations in sample mixing by centering the log₂ protein abundance ratio distribution over zero, as described in Dephoure et al. (2014). When calculating the normalization factor, proteins on the disomic chromosomes were excluded. We expect most proteins (except those on the disomic chromosome) to be present at a one-to-one ratio.

Calculation of expectation value for protein abundance ratio in Figure 1A–D after chromosome mis-segregation—While mis-segregation occurs in many of the cells in the population, mis-segregation itself and the isolation of disomic cells are not fully efficient. One hour following chromosome mis-segregation, the biotin-labeled purified cell culture contained 67% cells disomic for chromosome IV, 20% euploid cells, and 13% cells lacking chromosome IV (nullisomes). Five hours following chromosome mis-segregation, the biotin-labeled purified population was comprised of 61% disomes, 34% euploid cells, and 5% nullisomes. The slight decrease in the proportion of disomic cells at the 5 hour time point compared to the 1 hour time point is likely due to the reduced proliferation rate of disome IV cells compared to euploid cells.

The expected ratio of proteins encoded on chromosome IV from disome IV and euploid control strains depends on two factors: 1) the percentage of disomes, euploid cells, and nullisomes, and 2) the rate of protein turnover from degradation versus dilution. Given the measured percent of each karyotype at one and five hours, an expected value for the protein abundance ratio can be calculated for different models of protein turnover. In the extreme where proteins are only diluted by proliferation (using proliferation rate measured in Figure 3A and correcting for the ratio compression; see below) one would expect a log₂ protein abundance of 0.12 at 1 hour and 0.28 at 5 hours. In the other extreme where protein turnover is instantaneous, the expectation is a log₂ protein abundance of 0.27 at 1 hour and 0.28 at 5 hours. One hour following chromosome mis-segregation, proteins encoded on chromosome IV were elevated compared to proteins encoded by the euploid chromosomes, with a mean log₂ protein abundance ratio of 0.21 for proteins on chromosome IV, compared to a mean of 0 for proteins on all other chromosomes (Figure 1C). Levels of chromosome IV-encoded

proteins increased further to a mean \log_2 protein abundance ratio of 0.32 five hours following chromosome mis-segregation (Figure 1D).

Calculation of expected ratios: Given that previous work showed that proteins encoded on disomic chromosomes exhibit a protein ratio of 2:1 versus proteins encoded by euploid chromosomes (Dephoure et al., 2014), we assumed that the observed \log_2 protein abundance ratio of 1.4 for proteins encoded on disomic chromosome IV was due to ratio compression. We can therefore calculate a ratio compression factor for our samples, which then can then

be used to calculate the actual ratio using the following formula $\frac{2+x}{1+x}=1.4$ which yields a ratio compression factor (x in the equation) of 1.66.

To calculate the expected \log_2 protein abundance ratio we first used the following relationship:

$$\text{ChromosomeContentInDisome} = \% \text{Disome} * \left(1 * 2^{-\left(\frac{\text{time}}{\text{growthrateofdisome}}\right)} + 2 * \left(1 - 2^{-\left(\frac{\text{time}}{\text{growthrateofdisome}}\right)} \right) \right) \\ + \% \text{Euploid} * (1) + \% \text{Nullisome} * \left(1 * 2^{-\left(\frac{\text{time}}{\text{growthrateofnullisome}}\right)} \right)$$

When protein turnover is high this relationship simplifies to:

$$\text{ChromosomeContentInDisome} = \% \text{Disome} * \left(2 * \left(1 - 2^{-\left(\frac{\text{time}}{\text{growthrateofdisome}}\right)} \right) \right) + \% \text{Euploid} * (1)$$

The expectation value for the \log_2 protein abundance ratio is calculated with the following formula

$$\log_2 \left(\frac{\text{ChromosomeContentInDisome} + 1.66}{1 + 1.66} \right)$$

Aneuploid colony size measurements—Cells were grown in YEP-R and then transferred to YEP-RG for 160 minutes to induce chromosome mis-segregation. Cells were then plated on YEP-D agar plates. Mother-daughter pairs that had just completed a cell division were separated by micromanipulation and allowed to grow into colonies at 30°C. Colony size was measured 40 – 48 hours later when colony size was still increasing exponentially. Euploid colonies were grown on the same plate and were either from a wild-type strain or from cells in the experimental strain that did not missegregate a chromosome. Colony area was measured using ImageJ. Experiment was performed 3 times with similar results. Data from one representative experimental replicate are shown in Figure 1E–F and Figure S1B.

To calculate aneuploid to euploid colony area ratio, euploid colony area was measured and averaged per plate, with a separate average for euploid mothers and euploid daughters. Euploid cells on the same plate as the aneuploid cells were used for analysis to control for

plate-to-plate variability. A value for each individual aneuploid colony was calculated as a ratio of the aneuploid colony area to the mean euploid colony area for euploid cells. For disomes and trisomes, the mean colony area for euploid mothers was used. For monosomes, the mean colony area for euploid daughters was used. Each circle in Figure 1F represents the mean of all aneuploid/euploid ratios for a particular karyotype. Error bars indicate the standard deviation of the aneuploid/euploid ratios, not accounting for error propagation from euploid cells.

Chromosome mis-segregation was confirmed by determining whether colonies could grow on plates lacking uracil. The inducible chromosome is marked with *URA3* at the conditional centromere, so colony pairs in which one colony (arising from the daughter cell) is auxotrophic for growth on uracil and the other colony (arising from the mother cell) is prototrophic for growth on uracil indicates that a chromosome mis-segregation event occurred. For aneuploid strains with severe fitness defects, colonies were grown at 30°C until colonies were large enough to test for uracil prototrophy via replica-plating. Colonies were also tested for growth on plates containing glycerol as the sole carbon source. Colonies that did not grow on this medium were excluded from analysis as they are respiratory deficient, which causes slow growth. Rarely, the inducible chromosome was segregated into the daughter cell instead of the mother; these mis-segregation events were excluded from analysis.

The colony mis-segregation assay in haploid cells was used to determine the chromosome mis-segregation rates presented in Figure S1B. The growth defects observed in monosomes were more severe than the growth defects observed in disomes and trisomes (Figures 1F, S1B). While the sizes of many monosomic colonies were less than 1% of the sizes of colonies formed by euploid cells after ~48 hours of growth, nearly all monosomic strains eventually formed colonies after many days of growth. The only monosomy that was inviable was chromosome XIII monosomy, due to monosomy of *TUB1* which is lethal (Katz et al., 1990). Disomy and trisomy were better tolerated than monosomy, with the exception of disomy VI and trisomy VI. These chromosomal gains are inviable due to an increase in *TUB2* copy number (Katz et al., 1990).

Live-cell imaging

Differentiating aneuploid from euploid cells in live-cell cell cycle analysis: For cell cycle analyses, aneuploid cells were differentiated from euploid cells by counting the number of GFP dots present in a cell. In all euploid strains, 1 GFP dot per cell indicates euploidy. For disomes and trisomes of single chromosomes, the presence of 2 GFP dots in the cell indicates disomy or trisomy while 1 GFP dot indicates euploidy. For disomes and trisomes of 2 chromosomes, 4 GFP dots indicate disomy or trisomy. For disomes and trisomes of 3 chromosomes, cells with 4, 5 or 6 GFP dots were scored as disomes and trisomes, as it was difficult to accurately count GFP dots at numbers greater than 4 dots per cell. For all monosomes (single or multiple chromosomes), 0 GFP dots per cell indicates monosomy. In all analyses, euploid cells were either from the wild-type control strain or from cells in the experimental strain that did not mis-segregate a chromosome.

Cell cycle analysis image acquisition: For inducible aneuploids, cells were grown in SC-R to mid-log phase then transferred to SC-RG and grown for 160 minutes to induce chromosome mis-segregation. Chronic disomic strains were grown in SC-D medium to mid-log phase. Then, for both inducible aneuploids and chronic disomes, cells were transferred to SC-D and layered on an agar pad (2% agarose, SC-D) affixed to a glass slide and covered with a cover slip. Cells were imaged at 5-minute intervals for 8–10 hours using a Zeiss Axio Observer-Z1 with a 63x objective (Carl Zeiss), equipped with a Zeiss Definite Focus module (Carl Zeiss) and a Hamamatsu ORCA-AG digital camera (Hamamatsu). Nine Z-stacks (0.6 microns apart) were acquired and maximally projected. MetaMorph software (Molecular Devices) was used for image acquisition and processing.

Cell cycle analysis data processing: For cell cycle analyses of aneuploid cells, approximately 20 aneuploid cells and 10 euploid cells were scored per experiment. One or two independent biological replicates were performed for each aneuploid strain. Data from one representative biological replicate for each aneuploid strain are shown in Figures 2, 3, 4, and 5 and Figures S2, S3, S4, and S5. As most cells were analyzed for multiple divisions, we analyzed between 20 – 80 cell divisions for most strains. See Table S1 for the number of cell cycle stages (n) analyzed in each experiment. G1 duration, S+early M phase duration, anaphase onset to cytokinesis duration, and division time (cytokinesis to cytokinesis) were measured for each cell following chromosome mis-segregation. Analyses of cells started either at bud emergence or at anaphase onset in the first division following chromosome mis-segregation. We were not able to image cells during the first G1 phase following chromosome mis-segregation because of the time needed to prepare the cells for imaging. Thus, division time analyses start in the second division following chromosome mis-segregation.

At the end of the time-lapse, cells that were in G1 and had spent at least 100 minutes in G1 were scored as arrested and included in G1 duration calculations. Cells that were in G1 at the end of the time-lapse and had spent less than 100 minutes in G1 were not considered arrested and excluded from analysis for calculating G1 duration. At the end of the time-lapse, cells that had passed bud emergence but had not reached anaphase onset and had spent at least 200 minutes in that stage were scored as arrested and included in S+early M phase duration calculations. Cells that had passed bud emergence at the end of the time-lapse and had not reached anaphase onset but had spent less than 200 minutes in this stage were not considered arrested and excluded from analysis for calculating S+early M phase duration.

To calculate standard deviation of cell populations and compare variance using the F-test, raw data (in minutes) were used (Figure 2B–E, Figure 3B,C,F,G,I–K, Figure 4D–G, Figure 5D–G, and Figure S4I–L). These analyses were done on the combined data from all divisions measured following chromosome mis-segregation for all cells of a given karyotype for a particular cell cycle stage (G1, S+early M phase, or division time duration). Aneuploid cells were compared to euploid cells from the same experiment to account for minor day-to-day variability.

In Figure 2A, Figure 3A,E, Figure 4A–C, Figure 5A–C, Figure S2B–D, Figure S3A–C,E–G, and Figure S4F–H, cell cycle measurements for aneuploid cells were normalized to euploid

cells from the same experiment to allow us to compare cell cycle measurements among experiments. Each aneuploid cell measurement for G1 duration, S+early M phase duration, anaphase duration, or total division time was taken as a ratio of the mean of all euploid cells for the same measurement from the same division. For example, the G1 duration measurement for an inducible aneuploid cell in its third division following chromosome mis-segregation would be normalized to the mean of the G1 duration for all euploid cells in the third division following chromosome mis-segregation. Normalization to the euploid strain controls for day-to-day variability in experiments and for changes in cell cycle durations upon shift from raffinose+galactose (SC-RG) as the carbon source to glucose (SC-D) as the carbon source. In the same manner, measurements of cell cycle duration in chronic disomes were normalized to euploid controls by cell cycle stage and division. Log₂ transformed aneuploid to euploid ratios are plotted in the figures.

In Figures 2F and 3D,H, the longest G1 or S+early M phases were removed from the aneuploid data set until the standard deviation of the aneuploid cell cycle stage was equal to that of the corresponding euploid cell cycle stage in the same experiment. Standard deviations were considered equal when no longer significantly different by the F-test. The percent of the total number of measured cell cycle stages (G1 or S+early M phase) that were removed to equalize standard deviations of euploid and aneuploid data is reported.

Galactose and stress response reporter analyses—All *GAL1pr-YFP*, *UPRE-GFP*, and *HSE-YFP* reporter experiments were performed in synthetic dropout medium containing 1.7g/L yeast nitrogen base (BD Difco), 1g/L monosodium glutamate, 200µg/mL Geneticin (G418), and histidine dropout complete supplement mix (Sunrise Science), plus carbon sources. In the galactose response experiments, outgrowth cultures were grown in synthetic dropout medium supplemented with 2% raffinose, and induction assays were performed in synthetic dropout base supplemented with 0.25% galactose and a two-fold gradient of glucose ranging from 1.0%–0.002% (including a 0% condition). For the stress response experiments, all cultures were grown in synthetic dropout medium supplemented with 2% glucose. All 30°C incubations for the *GAL1pr-YFP*, *UPRE-GFP*, and *HSE-YFP* reporter experiments were performed in a humidified incubator (Infor Multitron) with rotary shaking at 230 rpm (tubes and flasks) or 999 rpm (deep 96-well plates). Higher-temperature incubations were conducted in an incubating microplate shaker (VWR) with rotary shaking at 1000rpm.

Galactose response assays—Strains were inoculated from colonies streaked on a G418/-his plate into liquid dropout medium supplemented with 2% glucose and incubated at 30°C for 24 hours until cultures reached saturation. Cultures were diluted 1:100 – 1:400 into medium containing 2% raffinose and grown for 16–18 hours. For the steady-state glucose gradient assay, raffinose cultures at a final OD₆₀₀ 0.1 were pelleted, washed twice, and then resuspended 1:1 in synthetic dropout medium without carbon and diluted 1:100 into the glucose gradient to measure expression of the *GAL1* reporter.

For the kinetic response assays, raffinose cultures with a final OD₆₀₀ 0.1–0.3 were selected; a 0 hour time point of the raffinose culture was harvested by addition of a concentrated TE/sodium azide 'stop solution' to a final (1X) concentration of 0.1% sodium azide. The

remaining culture was pelleted, washed twice, and then resuspended at a 1:4 dilution into G418/-his liquid medium supplemented with 2% galactose. Aliquots were harvested every 30 min for up to 8 hours after the medium switch, and at 9 and 10 hours post medium switch.

Dual-reporter noise assay—Strains bearing a tandem *GAL1pr-YFP-TDH3pr-mCherry* reporter were inoculated from colonies streaked on a G418/-his plate into liquid dropout medium supplemented with 2% glucose and incubated at 30°C for 24 hours until cultures reached saturation. Cultures were diluted 1:200 into medium supplemented with 2% galactose and grown to saturation. Cultures were then diluted 1:10 into fresh 2% galactose medium and grown for 8 hours before they were analyzed by flow cytometry. Each strain was measured in eight replicates.

Stress response assays—Strains were inoculated from colonies streaked on a G418/-his plate into liquid G418/-his medium and incubated at 30°C for 24 hours until cultures reached saturation. Cultures were diluted 1:100–1:400 and grown for 8–12 hours until they reached an OD₆₀₀ of ~0.1–0.2.

For the heat-shock experiment, the outgrowth cultures were diluted 1:50 into pre-warmed medium in a 96 deep well plate and grown for 4 hours with rotary shaking at the specified temperature. After incubation, cultures were pelleted by centrifugation, washed twice, and resuspended in Tris-EDTA pH 7.5 (TE) before analysis on the flow cytometer.

For the DTT stress response experiments, the outgrowth cultures were diluted 1:4 into medium containing a final concentration of either 0.625mM DTT or a 2-fold serial dilution ranging from 10–0.0098mM (including a 0mM condition). All cultures were grown for 4 hours at 30°C before being harvested by addition of concentrated TE/sodium azide 'stop solution' to a final (1X) concentration of 0.1% sodium azide.

Flow cytometry and data analysis—All samples were run on a Stratadigm S1000EX cytometer with FSC/SSC thresholds set to 200. PMT gain settings of FITC 0.5%, FSC 34.3%, SSC 40.0% were used for the dual-reporter noise assay. PMT gain settings of FITC 2.0%, FSC 33.5%, SSC 55.3% were used for all other assays. Flow cytometry data were analyzed using custom MATLAB code (<https://github.com/springerlab/Flow-Cytometry-Toolkit>). As a general workflow, raw FCS data were processed by gating out debris and bacterial contamination events based on FSC/SSC measurements, normalizing the YFP values to cell size by dividing by SSC values, rescaling the values by an arbitrary factor of 10^{3.5} for visualization purposes, and computing population statistics, expression histograms, and other metrics of induction from the log₁₀-transformed data.

For the steady-state galactose and stress response experiments, induced fractions were calculated relative to the probability distribution of cells grown only in glucose-containing medium in the absence of stressors (see Figure S8; Escalante-Chong et al., 2015). Separate “off”, “inducing”, and “on” fractions were similarly defined relative to the probability distributions from maximally induced and uninduced conditions (see Figure S8), with threshold concentrations being calculated from a cubic spline (MATLAB function `csaps`)

with smoothing parameter of 0.9) that was fit to the data by interpolating between consecutive points of normalized log-transformed YFP values plotted against concentration (glucose or DTT).

Mouse embryo imaging and analysis—To isolate embryos of a certain gestational stage, the day on which a copulatory plug was observed was defined as embryonic day E0.5. Embryos were collected at the indicated gestational stages. Amniotic membranes and portions of the umbilical cords were carefully removed, and embryos were rinsed twice with PBS before placing them on a 10-cm petri dish for imaging. A Canon EF 100mm f/2.8L Macro IS USM lens was used to attain the close-up magnification of 1x at the closest focusing. Aperture-stop was chosen to cover sufficient depth of field while keeping the macrophotography diffraction limited. Thickness of the nuchal edema, defined as the translucent region in the neck and head region, was measured in the region of the embryo, where the width was maximal. The nuchal edema thickness of an embryo, in pixel number, was calculated using the Ruler Tool in Adobe Photoshop 6.0, and then converted to metrics given the pixel pitch of the camera sensor.

Experimental design—In regard to experimental design, replication was not performed. Randomization and/or stratification were not used, as in all experiments the same experimental conditions were performed on cells or embryos of different genotypes. No blinding was done at any stage of the study. All data points were included in analysis unless otherwise noted (see “Cell cycle analysis data processing” section above for criteria used to score cells as arrested). Sample size estimation was not performed computationally; instead, experiments were designed to maximize the number of cells or embryos analyzed that was technically feasible.

QUANTIFICATION AND STATISTICAL ANALYSIS

Protein quantification by mass spectrometry—For the quantification of the proteome of aneuploid yeast following chromosome mis-segregation shown in Figure 1A–D, one biological replicate ($n = 1$) was performed with three technical replicates (see Methods Details).

Aneuploid colony size measurements—Aneuploid colony size measurements shown in Figure 1F and Figure S1B were calculated as described above in Methods Details. Linear regressions and p values (testing deviation from zero for the slope of the linear regression) in Figure 1F were calculated using GraphPad Prism 6 software. No methods were used to test whether the data met assumptions of the statistical approach. The n values shown in Figure S1B indicate the numbers of aneuploid colonies measured for data shown in Figure 1F and Figure S1B.

Cell cycle analysis—In Figure 2B–C, Figure 3B,C,F,G, Figure 4D–G, Figure 5D–G, and Figure S4I–L, statistical significance of variability was assessed by F tests on the values of each given metric (G1 and S+early M phase durations) using GraphPad Prism 6 software. No methods were used to test whether the data met assumptions of the statistical approach. The “n” values for each measurement represent the number of cell cycle stages analyzed (for

instance, $n = 45$ indicates 45 G1 phase lengths) and are listed in Table S1. The “ n ” values for comparisons of division lengths in subsequent cell divisions in Figure S4A–E and Figure S5 are found in the legends for these figures. Linear regressions and p values (testing deviation from zero for the slope of the linear regression) in Figure S2E, Figure S3D, Figure S4A–E and Figure S5 were calculated using GraphPad Prism 6 software. One or two independent biological replicates were performed for each aneuploid strain.

Galactose induction and stress response assays—For analyses conducted in Figure 6A–F and Figure S6 (all galactose induction and stress response assays), statistical significance of variability between wild-type and aneuploid strains was assessed by two-sided Wilcoxon rank sum tests on the values of each given metric (mean expression level and standard deviation of the expression level). Results of the significance testing are summarized in Table S2. No methods were used to determine whether the data met assumptions of the statistical approaches used; however, the statistical approaches used do not assume normality. At least 4 independent biological replicates ($n = 4$) were performed for all galactose induction and stress response assays.

Dual reporter variability assay—For the dual-reporter variability assay (Figure 6G), data were analyzed using customized MATLAB code. For each sample, all events were equally binned into 30 bins by SSC, as a proxy for cell size. Events from each bin were treated as if they were from cells with similar cell sizes. The Pearson correlation coefficients between mCherry and YFP were calculated for events in each SSC bin, and averaged among bins representing intermediate cell sizes, defined as 40~60 percentile. Statistical significance between aneuploid and euploid cells was assessed by Wilcoxon rank sum tests on the correlation values. No methods were used to determine whether the data met assumptions of the statistical approaches used; however, the statistical approaches used do not assume normality. Four independent biological replicates ($n = 4$) were performed.

Nuchal edema measurements—To determine whether the difference in variance in nuchal edema thickness (Figure 7B) was statistically significant, we performed two statistical tests: 1) we calculated an F-statistic on the variance ($p < 0.005$), and 2) we permuted all the nuchal edema thickness values, randomly split them into two groups ('wt' and 'trisomy 19') and determined whether the variance was at least as large as observed in the real data (39500 out of 1,000,000, or $p = 0.0395$). No methods were used to determine whether the data met assumptions of the statistical approach. One experimental replicate was performed due to the difficulty in obtaining trisomic embryos. For the nuchal edema thickness measurements shown in Figure 7B, $n = 14$ for euploid (WT) embryos and $n = 6$ for trisomy 19 (Ts19) embryos.

DATA AND SOFTWARE AVAILABILITY

The mass spectrometry proteomics dataset in Figure 1A–D is available for download from ProteomeXchange (Accession: PXD006009; DOI: 10.6019/PXD006009). The flow cytometry datasets in Figure 6, Figure 7, Figure S6 and Figure S7 are available for download from Dryad (doi:10.5061/dryad.30mv0).

KEY RESOURCES TABLE

REAGENT or RESOURCE	SOURCE	IDENTIFIER
Chemicals, Peptides, and Recombinant Proteins		
α -factor yeast mating pheromone	The Koch Institute Swanson Biotechnology Center – Biopolymers Core Facility	N/A
Streptavidin, Alexa Fluor 568 conjugate	Molecular Probes	Cat#S11226
EZ-Link Sulfo-NHS-LC-Biotin	Thermo Scientific	Cat#21335
YEP-R (yeast extract peptone + 2% raffinose)	Amon lab	N/A
YEP-RG (yeast extract peptone + 2% raffinose + 2% galactose)	Amon lab	N/A
YEP-D (yeast extract peptone + 2% glucose)	Amon lab	N/A
SC-R (synthetic complete medium + 2% raffinose)	Amon lab	N/A
SC-RG (synthetic complete medium + 2% raffinose + 2% galactose)	Amon lab	N/A
SC-D (synthetic complete medium + 2% glucose)	Amon lab	N/A
Yeast nitrogen base	BD Difco	Cat#BD233520
Histidine dropout complete supplement mix	Sunrise Science	Cat#1006-010
Geneticin (G418)	Gibco	Cat#11811023
Critical Commercial Assays		
Anti-Biotin MicroBeads	Miltenyi Biotec	Cat#130-090-485
LS Columns	Miltenyi Biotec	Cat#130-042-401
Pre-Separation Filters (30 μ m)	Miltenyi Biotec	Cat#130-041-407
QuadroMACS Separator	Miltenyi Biotec	Cat#130-090-976
MACS MultiStand	Miltenyi Biotec	Cat#130-042-303
FastPrep-24	MP Biomedicals	N/A
Bradford protein assay	Bio-Rad	Cat#5000006
Thermo Q Exactive mass spectrometer	Thermo Scientific	N/A
Stratedigm S1000EX cytometer	Stratedigm	N/A
Deposited Data		
Mass spectrometry proteomics data	ProteomeXchange consortium via the PRIDE partner repository	ProteomeXchange Accession: PXD006009; DOI: 10.6019/PXD006009
Flow cytometry data	Dryad	doi:10.5061/dryad.30mv0
Experimental Models: Organisms/Strains		
All <i>Saccharomyces cerevisiae</i> strains used in this study are of the W303 strain background and are listed in Table S3.	N/A	N/A

REAGENT or RESOURCE	SOURCE	IDENTIFIER
Mouse: C57BL/6J	The Jackson Laboratory	JAX 000664
Mouse: B6.Cg-Rb(5.19)1Wh/JAmonJ	Amon lab, The Jackson Laboratory	JAX 014113
Mouse: B6Ei.Cg-Rb(9.19)163H/J	Amon lab	N/A
Mouse: B6.Cg-Rb(11.13)4Bnr/JAmonJ	Amon lab	N/A
Mouse: B6.Cg-Rb(13.16)1Mpl/JAmonJ	Amon lab, The Jackson Laboratory	JAX 014118
Oligonucleotides		
Primers used to generate inducible aneuploid strains are listed in Table S4.	N/A	N/A
Recombinant DNA		
Plasmids used to generate inducible aneuploid strains are listed in Table S5.	N/A	N/A
Plasmid: <i>YIp211-CDC3-mCherry</i>	Fang et al. (2010)	N/A
Plasmid: <i>GAL1pr-YFP</i>	Escalante-Chong et al. (2015)	N/A
Plasmid: <i>P_{4xHSE}-YFP</i>	Damon et al. (2015)	N/A
Plasmid: <i>P_{4xUPRE}-GFP</i>	Damon et al. (2015)	N/A
Construct: <i>TDH3pr-mCherry</i>	Springer lab	N/A
Software and Algorithms		
MATLAB code to analyze flow cytometry data	This paper	https://github.com/springerlab/Flow-Cytometry-Toolkit
MATLAB	MathWorks	https://www.mathworks.com/
GraphPad Prism 6.0	GraphPad Software	http://www.graphpad.com
ImageJ	NIH	https://imagej.nih.gov/ij/
Mascot	Matrix Science	http://www.matrixscience.com/
MetaMorph	Molecular Devices	https://www.moleculardevices.com/
Adobe Photoshop 6.0 (Ruler Tool)	Adobe	http://www.photoshop.com/

Supplementary Material

Refer to Web version on PubMed Central for supplementary material.

Acknowledgments

We thank Kirk Anders, Doug Koshland and David Pincus for reagents and the Koch Institute Swanson Biotechnology Center for technical support, specifically the Biopolymers & Proteomics Core Facility. This work was supported by the National Institutes of Health (CA206157-22 and GM118066 to A.A.), in part by the Koch Institute Support Grant P30-CA14051, National Science Foundation Graduate Research Fellowships (C.R., C.M.) and a National Science Foundation grant 1349248 (M.S. and B.H.). A.A. is an investigator of the Howard Hughes Medical Institute and of the Glenn Foundation for Biomedical Research.

References

Acar M, Mettetal JT, van Oudenaarden A. Stochastic switching as a survival strategy in fluctuating environments. *Nat Genet.* 2008; 40:471–475. [PubMed: 18362885]

- Alvaro D, Sunjevaric I, Reid RJD, Lisby M, Stillman DJ, Rothstein R. Systematic hybrid LOH: a new method to reduce false positives and negatives during screening of yeast gene deletion libraries. *Yeast Chichester Engl.* 2006; 23:1097–1106.
- Anders KR, Kudrna JR, Keller KE, Kinghorn B, Miller EM, Pauw D, Peck AT, Shellooe CE, Strong IJT. A strategy for constructing aneuploid yeast strains by transient nondisjunction of a target chromosome. *BMC Genet.* 2009; 10:36. [PubMed: 19594932]
- Arias AM, Hayward P. Filtering transcriptional noise during development: concepts and mechanisms. *Nat Rev Genet.* 2006; 7:34–44. [PubMed: 16369570]
- Axelrod K, Sanchez A, Gore J. Phenotypic states become increasingly sensitive to perturbations near a bifurcation in a synthetic gene network. *eLife.* 2015:4.
- Beaumont HJE, Gallie J, Kost C, Ferguson GC, Rainey PB. Experimental evolution of bet hedging. *Nature.* 2009; 462:90–93. [PubMed: 19890329]
- Blake WJ, KÆrn M, Cantor CR, Collins JJ. Noise in eukaryotic gene expression. *Nature.* 2003; 422:633–637. [PubMed: 12687005]
- Blank HM, Sheltzer JM, Meehl CM, Amon A. Mitotic entry in the presence of DNA damage is a widespread property of aneuploidy in yeast. *Mol Biol Cell.* 2015; 26:1440–1451. [PubMed: 25694455]
- Bonney ME, Moriya H, Amon A. Aneuploid proliferation defects in yeast are not driven by copy number changes of a few dosage-sensitive genes. *Genes Dev.* 2015; 29:898–903. [PubMed: 25934502]
- Bressan DA, Vazquez J, Haber JE. Mating type-dependent constraints on the mobility of the left arm of yeast chromosome III. *J Cell Biol.* 2004; 164:361–371. [PubMed: 14745000]
- Cerulus B, New AM, Pougach K, Verstrepen KJ. Noise and Epigenetic Inheritance of Single-Cell Division Times Influence Population Fitness. *Curr Biol CB.* 2016; 26:1138–1147. [PubMed: 27068419]
- Chen G, Mulla WA, Kucharavy A, Tsai HJ, Rubinstein B, Conkright J, McCroskey S, Bradford WD, Weems L, Haug JS, et al. Targeting the Adaptability of Heterogeneous Aneuploids. *Cell.* 2015; 160:771–784. [PubMed: 25679766]
- Christoforou AL, Lilley KS. Isobaric tagging approaches in quantitative proteomics: the ups and downs. *Anal Bioanal Chem.* 2012; 404:1029–1037. [PubMed: 22580419]
- Damon JR, Pincus D, Ploegh HL. tRNA thiolation links translation to stress responses in *Saccharomyces cerevisiae*. *Mol Biol Cell.* 2015; 26:270–282. [PubMed: 25392298]
- Dephoure N, Hwang S, O’Sullivan C, Dodgson SE, Gygi SP, Amon A, Torres EM. Quantitative proteomic analysis reveals posttranslational responses to aneuploidy in yeast. *eLife.* 2014; 3:e03023. [PubMed: 25073701]
- Deutschbauer AM. Mechanisms of Haploinsufficiency Revealed by Genome-Wide Profiling in Yeast. *Genetics.* 2005; 169:1915–1925. [PubMed: 15716499]
- Donaldson AD, Kilmartin JV. Spc42p: a phosphorylated component of the *S. cerevisiae* spindle pole body (SPB) with an essential function during SPB duplication. *J Cell Biol.* 1996; 132:887–901. [PubMed: 8603920]
- Elowitz MB, Levine AJ, Siggia ED, Swain PS. Stochastic gene expression in a single cell. *Science.* 2002; 297:1183–1186. [PubMed: 12183631]
- Escalante-Chong R, Savir Y, Carroll SM, Ingraham JB, Wang J, Marx CJ, Springer M. Galactose metabolic genes in yeast respond to a ratio of galactose and glucose. *Proc Natl Acad Sci U S A.* 2015; 112:1636–1641. [PubMed: 25605920]
- Fang X, Luo J, Nishihama R, Wloka C, Dravis C, Travaglia M, Iwase M, Vallen EA, Bi E. Biphasic targeting and cleavage furrow ingression directed by the tail of a myosin II. *J Cell Biol.* 2010; 191:1333–1350. [PubMed: 21173112]
- Fridman O, Goldberg A, Ronin I, Shores N, Balaban NQ. Optimization of lag time underlies antibiotic tolerance in evolved bacterial populations. *Nature.* 2014; 513:418–421. [PubMed: 25043002]
- Goldstein AL, McCusker JH. Three new dominant drug resistance cassettes for gene disruption in *Saccharomyces cerevisiae*. *Yeast Chichester Engl.* 1999; 15:1541–1553.

- Guthrie, C., Fink, G. Guide to yeast genetics and molecular biology. San Diego, Calif: Acad. Press; 1991.
- Henrichsen CN, Chaignat E, Reymond A. Copy number variants, diseases and gene expression. *Hum Mol Genet.* 2009; 18:R1–R8. [PubMed: 19297395]
- Herrero, E., Angeles de la Torre, M., Torres, J., Belli, G. Regulation of G1 phase of yeast cells by stress. In: Boonstra, J., editor. In G1 Phase Progression. New York: Kluwer Academic/Plenum; 2003. p. 165-186.
- Hickman MA, Paulson C, Dudley A, Berman J. Parasexual Ploidy Reduction Drives Population Heterogeneity Through Random and Transient Aneuploidy in *Candida albicans*. *Genetics.* 2015; 200:781–794. [PubMed: 25991822]
- Hill A, Bloom K. Genetic manipulation of centromere function. *Mol Cell Biol.* 1987; 7:2397–2405. [PubMed: 3302676]
- Huh D, Paulsson J. Non-genetic heterogeneity from stochastic partitioning at cell division. *Nat Genet.* 2011; 43:95–100. [PubMed: 21186354]
- Jajoo R, Jung Y, Huh D, Viana MP, Rafelski SM, Springer M, Paulsson J. Accurate concentration control of mitochondria and nucleoids. *Science.* 2016; 351:169–172. [PubMed: 26744405]
- Kashiwagi A, Urabe I, Kaneko K, Yomo T. Adaptive response of a gene network to environmental changes by fitness-induced attractor selection. *PLoS One.* 2006; 1:e49. [PubMed: 17183678]
- Katz W, Weinstein B, Solomon F. Regulation of tubulin levels and microtubule assembly in *Saccharomyces cerevisiae*: consequences of altered tubulin gene copy number. *Mol Cell Biol.* 1990; 10:5286–5294. [PubMed: 2204811]
- Kim HB, Haarer BK, Pringle JR. Cellular morphogenesis in the *Saccharomyces cerevisiae* cell cycle: localization of the CDC3 gene product and the timing of events at the budding site. *J Cell Biol.* 1991; 112:535–544. [PubMed: 1993729]
- Levy SF, Ziv N, Siegal ML. Bet hedging in yeast by heterogeneous, age-correlated expression of a stress protectant. *PLoS Biol.* 2012; 10:e1001325. [PubMed: 22589700]
- Longtine MS, McKenzie A, Demarini DJ, Shah NG, Wach A, Brachat A, Philippsen P, Pringle JR. Additional modules for versatile and economical PCR-based gene deletion and modification in *Saccharomyces cerevisiae*. *Yeast Chichester Engl.* 1998; 14:953–961.
- Mileyko Y, Joh RI, Weitz JS. Small-scale copy number variation and large-scale changes in gene expression. *Proc Natl Acad Sci.* 2008; 105:16659–16664. [PubMed: 18946033]
- Miller MP, Unal E, Brar GA, Amon A. Meiosis I chromosome segregation is established through regulation of microtubule-kinetochore interactions. *eLife.* 2012; 1:e00117. [PubMed: 23275833]
- Murray AW, Szostak JW. Pedigree analysis of plasmid segregation in yeast. *Cell.* 1983; 34:961–970. [PubMed: 6354471]
- Nicholson JM, Macedo JC, Mattingly AJ, Wangsa D, Camps J, Lima V, Gomes AM, Dória S, Ried T, Logarinho E, et al. Chromosome mis-segregation and cytokinesis failure in trisomic human cells. *eLife.* 2015; 4
- Passerini V, Ozeri-Galai E, de Pagter MS, Donnelly N, Schmalbrock S, Kloosterman WP, Kerem B, Storchová Z. The presence of extra chromosomes leads to genomic instability. *Nat Commun.* 2016; 7:10754. [PubMed: 26876972]
- Paulsson J. Summing up the noise in gene networks. *Nature.* 2004; 427:415–418. [PubMed: 14749823]
- Pfau SJ, Amon A. A System to Study Aneuploidy In Vivo. *Cold Spring Harb Symp Quant Biol.* 2015; 80:93–101. [PubMed: 26936868]
- Raj A, van Oudenaarden A. Nature, nurture, or chance: stochastic gene expression and its consequences. *Cell.* 2008; 135:216–226. [PubMed: 18957198]
- Rancati G, Pavelka N, Fleharty B, Noll A, Trimble R, Walton K, Perera A, Staehling-Hampton K, Seidel CW, Li R. Aneuploidy underlies rapid adaptive evolution of yeast cells deprived of a conserved cytokinesis motor. *Cell.* 2008; 135:879–893. [PubMed: 19041751]
- Raser JM, O’Shea EK. Noise in gene expression: origins, consequences, and control. *Science.* 2005; 309:2010–2013. [PubMed: 16179466]

- Roper RJ, Reeves RH. Understanding the Basis for Down Syndrome Phenotypes. *PLoS Genet.* 2006; 2:e50. [PubMed: 16596169]
- Sandler O, Mizrahi SP, Weiss N, Agam O, Simon I, Balaban NQ. Lineage correlations of single cell division time as a probe of cell-cycle dynamics. *Nature.* 2015; 519:468–471. [PubMed: 25762143]
- Sheltzer JM, Blank HM, Pfau SJ, Tange Y, George BM, Humpton TJ, Brito IL, Hiraoka Y, Niwa O, Amon A. Aneuploidy drives genomic instability in yeast. *Science.* 2011; 333:1026–1030. [PubMed: 21852501]
- Siegel JJ, Amon A. New insights into the troubles of aneuploidy. *Annu Rev Cell Dev Biol.* 2012; 28:189–214. [PubMed: 22804579]
- Sigal A, Milo R, Cohen A, Geva-Zatorsky N, Klein Y, Liron Y, Rosenfeld N, Danon T, Perzov N, Alon U. Variability and memory of protein levels in human cells. *Nature.* 2006; 444:643–646. [PubMed: 17122776]
- Smeal T, Claus J, Kennedy B, Cole F, Guarente L. Loss of transcriptional silencing causes sterility in old mother cells of *S. cerevisiae*. *Cell.* 1996; 84:633–642. [PubMed: 8598049]
- Stingele S, Stoehr G, Peplowska K, Cox J, Mann M, Storchova Z. Global analysis of genome, transcriptome and proteome reveals the response to aneuploidy in human cells. *Mol Syst Biol.* 2012; 8:608. [PubMed: 22968442]
- Straight AF, Belmont AS, Robinett CC, Murray AW. GFP tagging of budding yeast chromosomes reveals that protein–protein interactions can mediate sister chromatid cohesion. *Curr Biol.* 1996; 6:1599–1608. [PubMed: 8994824]
- Thorburn RR, Gonzalez C, Brar GA, Christen S, Carlile TM, Ingolia NT, Sauer U, Weissman JS, Amon A. Aneuploid yeast strains exhibit defects in cell growth and passage through START. *Mol Biol Cell.* 2013; 24:1274–1289. [PubMed: 23468524]
- Torres EM, Sokolsky T, Tucker CM, Chan LY, Boselli M, Dunham MJ, Amon A. Effects of aneuploidy on cellular physiology and cell division in haploid yeast. *Science.* 2007; 317:916–924. [PubMed: 17702937]
- Torres EM, Dephore N, Panneerselvam A, Tucker CM, Whittaker CA, Gygi SP, Dunham MJ, Amon A. Identification of aneuploidy-tolerating mutations. *Cell.* 2010; 143:71–83. [PubMed: 20850176]
- Uphoff S, Lord ND, Okumus B, Potvin-Trottier L, Sherratt DJ, Paulsson J. Stochastic activation of a DNA damage response causes cell-to-cell mutation rate variation. *Science.* 2016; 351:1094–1097. [PubMed: 26941321]
- Weinert T, Hartwell L. The RAD9 gene controls the cell cycle response to DNA damage in *Saccharomyces cerevisiae*. *Science.* 1988; 241:317–322. [PubMed: 3291120]
- Williams BR, Prabhu VR, Hunter KE, Glazier CM, Whittaker CA, Housman DE, Amon A. Aneuploidy affects proliferation and spontaneous immortalization in mammalian cells. *Science.* 2008; 322:703–709. [PubMed: 18974345]
- Zhu J, Pavelka N, Bradford WD, Rancati G, Li R. Karyotypic determinants of chromosome instability in aneuploid budding yeast. *PLoS Genet.* 2012; 8:e1002719. [PubMed: 22615582]

HIGHLIGHTS

- Non-genetic individuality is a universal characteristic of the aneuploid state
- Chromosome-scale changes in gene dosage decrease robustness of biological networks
- Cells with same aneuploid karyotype show cell cycle and gene expression variability
- Inbred trisomic mouse embryos exhibit variability in morphology

CONTEXT AND SIGNIFICANCE OF THE FINDINGS

We find that whole chromosome gains and losses, known as aneuploidy, cause non-genetic phenotypic variability. Yeast cell populations harboring the same defined aneuploidy exhibit heterogeneity in cell cycle progression, gene induction and stress response. Inbred aneuploid mouse embryos also show variable phenotypes. We conclude that while subtle changes in dosage of individual genes have little effect on the robustness of biological networks, gene dosage changes can promote alternate behaviors when they occur at a large scale. We propose that non-genetic individuality contributes to variability in presentation and treatment responses of diseases caused by aneuploidy such as cancer and Down Syndrome.

Author Manuscript

Author Manuscript

Author Manuscript

Author Manuscript

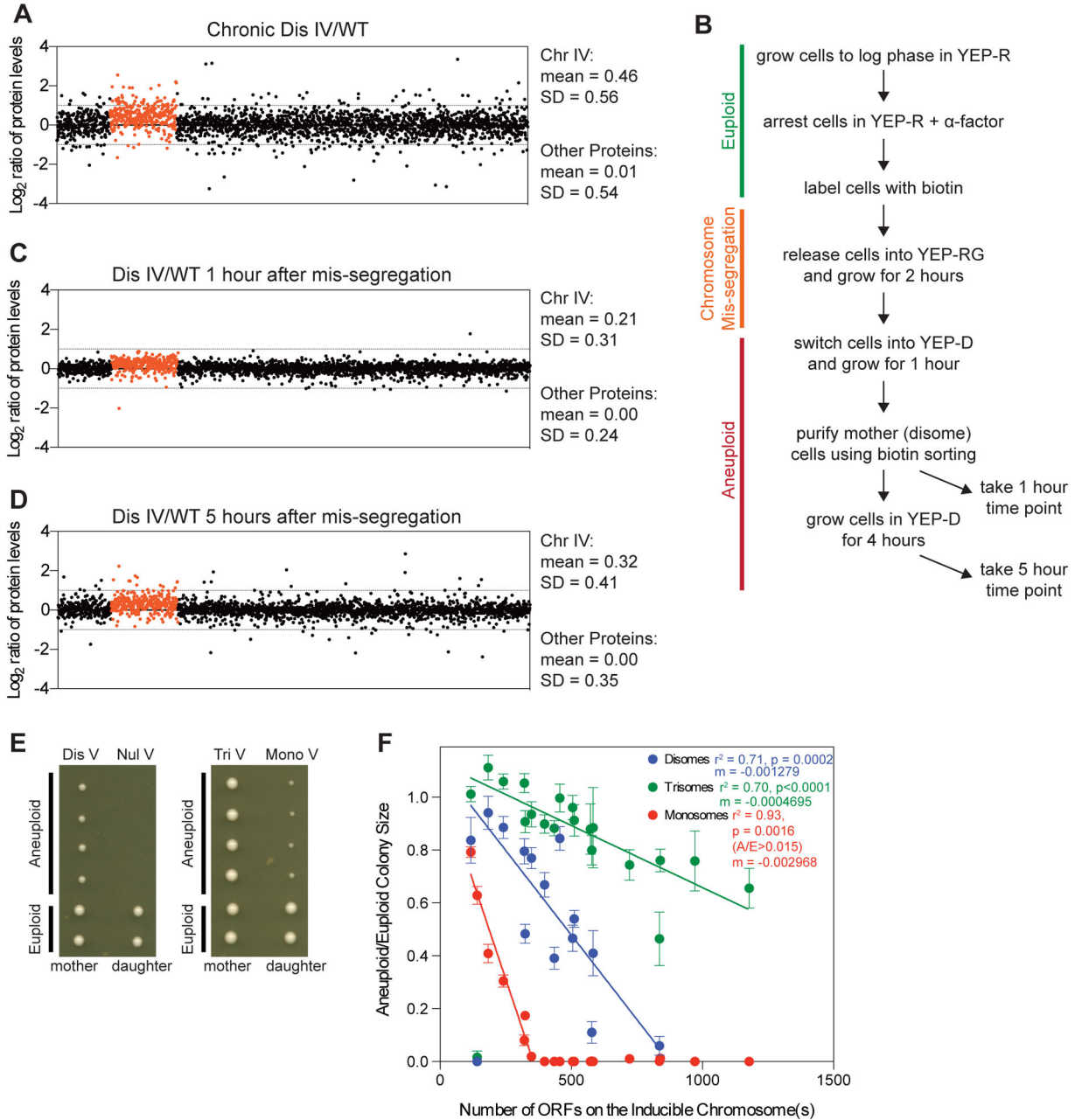


Figure 1. The proteome rapidly adjusts to changes in gene dosage

(A) Log₂ ratio of the relative protein abundance of chronic disome (Dis) IV compared to euploid (WT) cells from the 5-hour time-point in (D).

(B) Experimental setup to compare proteome 1 (C) and 5 (D) hours following chromosome mis-segregation.

(C,D) Log₂ ratios of the relative protein abundance of disome IV cells compared to euploid cells 1 (C) and 5 (D) hours following chromosome mis-segregation. Proteins encoded on chromosome (Chr) IV are red in (A), (C) and (D).

(E–F) Following chromosome mis-segregation, mother-daughter cell pairs were placed side-by-side on YEP-D plates. Colony area was measured after growth for 40–48 hours. Error bars indicate standard deviation (SD). Linear regressions ($m = \text{slope}$) exclude disome and trisome VI due to lethality of excess *TUB2* and only include monosomes with aneuploid to euploid ratios (A/E) > 0.015 .

Abbreviations: Nul, nullisome; Tri, trisome; Mono, monosome. See also Figure S1.

Author Manuscript

Author Manuscript

Author Manuscript

Author Manuscript

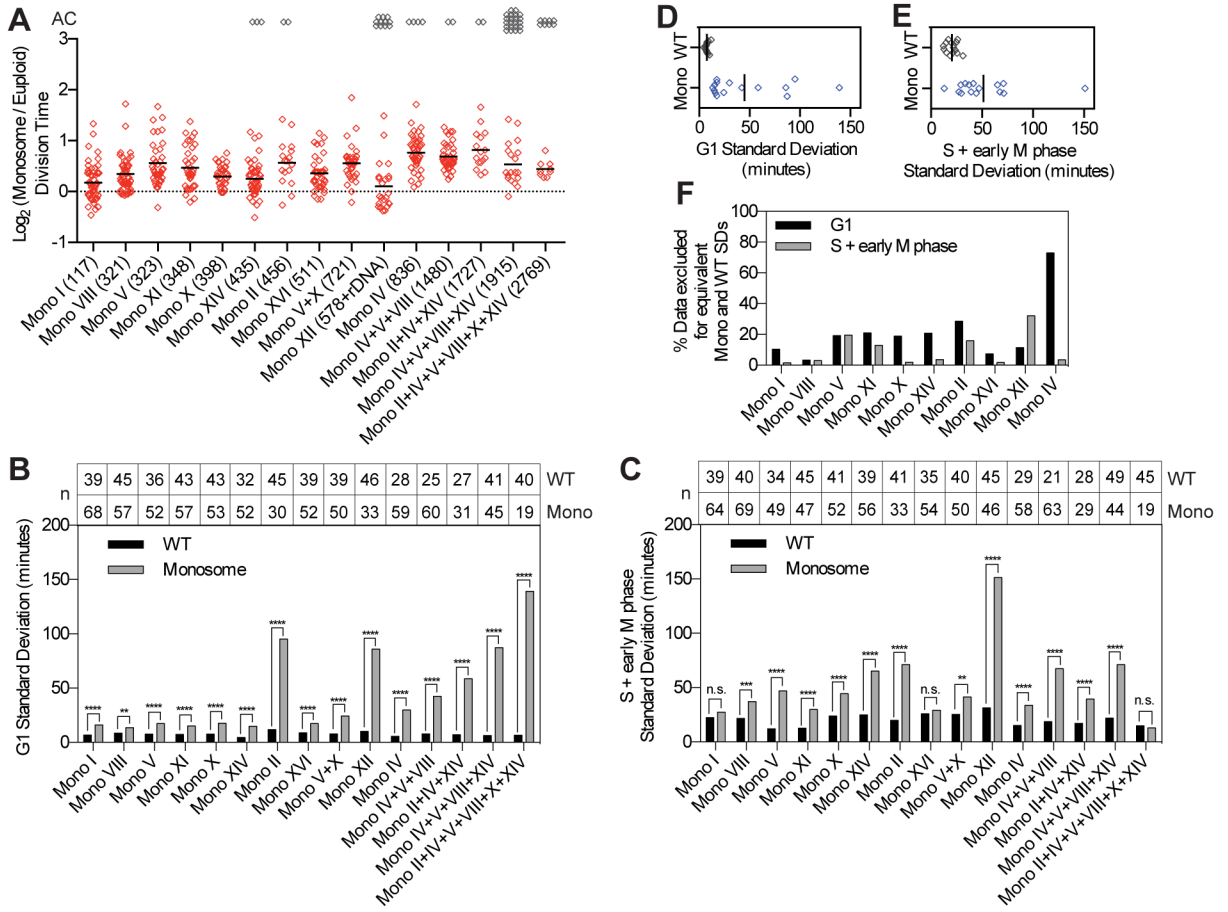


Figure 2. Chromosome loss leads to cell cycle delays and cell-to-cell variability
 (A–F) Following induction of chromosome mis-segregation, cells were imaged every 5 minutes for 8–10 hours. Division time (A) was calculated for monosomes (Mono) and normalized to euploid (WT) cells imaged during the same time-lapse. Log₂ aneuploid to euploid ratios are plotted with lines at the mean. “AC” indicates arrested cells. Numbers on the x-axis labels indicate number of open reading frames on the aneuploid chromosome(s). Standard deviations (B–E) were measured and an F-test was used to test for equality of variance between the monosome and the euploid population from the same experiment (** = p 0.01, *** = p 0.001, **** = p 0.0001).
 (F) The number of most slowly dividing cells (as percent of the total population) that need to be excluded from the monosome population to obtain equal variance with the euploid population is shown for G1 and S+early M phase. Note that we did not analyze strains harboring multiple monosomies. Many of these cells only undergo 1–2 cell divisions before arresting, which underreports variability as long-lived proteins have not yet adjusted to the monosomic state and thus have not yet become limiting. See also Figure S2 and Table S1.

Author Manuscript

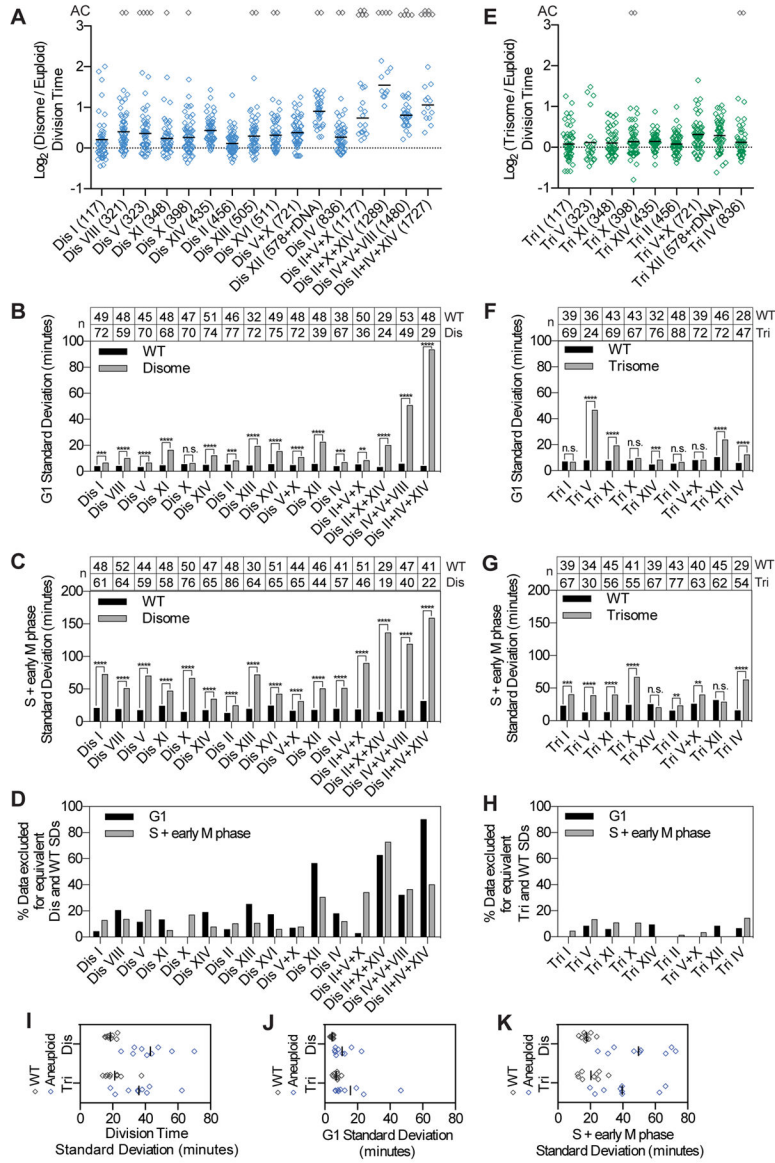


Figure 3. Chromosome gain leads to cell-to-cell variability that is partially attenuated by increased ploidy
 Cells were grown and imaged and disome (Dis) division times (A) and standard deviations (B,C,I-K) and trisome (Tri) division times (E) and standard deviations (F,G,I-K) were calculated as described in Figure 2 (** = $p < 0.01$, *** = $p < 0.001$, **** = $p < 0.0001$). The number of most slowly dividing cells (as percent of the total population) that need to be excluded from the disome (D) or trisome (H) population to obtain equal variance with the euploid population is shown for G1 and S+early M phase. Plots in I–K show only common aneuploidies between disomes and trisomes (chromosomes I, II, IV, V, X, XI, XII, XIV, and V+X). See also Figure S3 and Table S1.

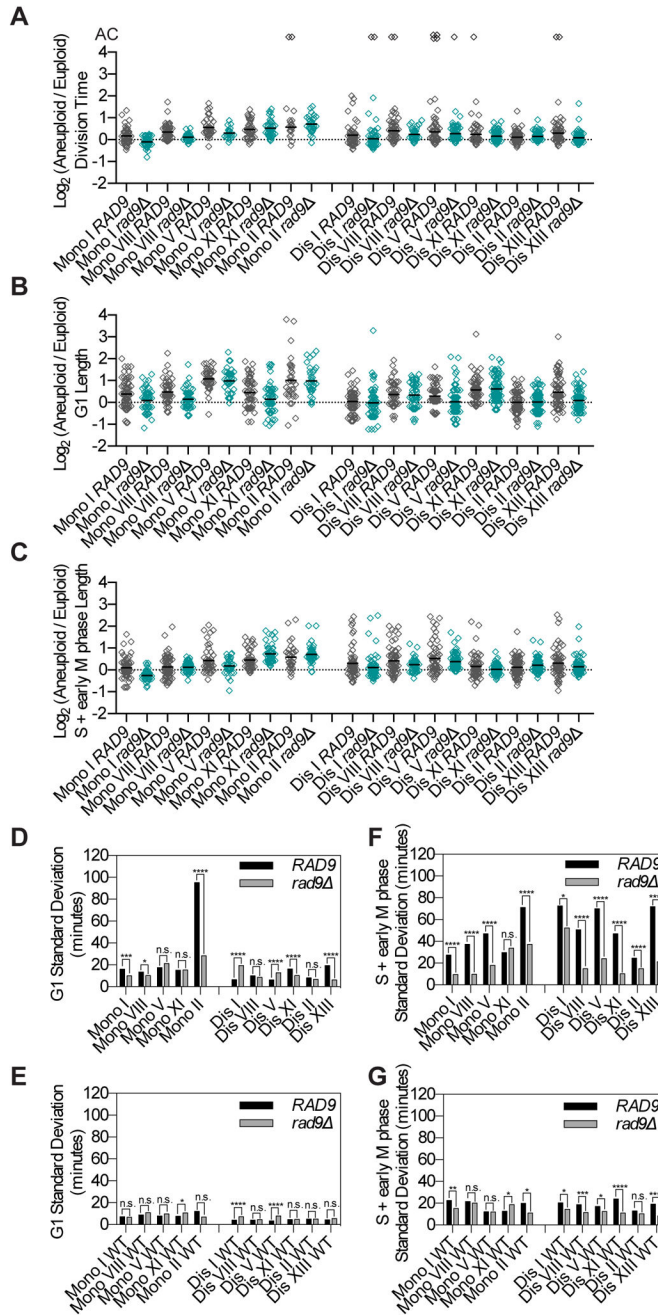


Figure 4. Cell-to-cell variability is in part due to stochastic DNA damage
 Cells were grown and imaged and division time (A), G1 length (B), and S+early M phase length (C) were calculated as described in Figure 2. Standard deviations for euploid (WT; E,G) and aneuploid (monosome, “Mono”; disome, “Dis”; D,F) populations were measured and an F-test was used to test for equality of variance between *RAD9* and *rad9Δ* populations (* = p < 0.05, ** = p < 0.01, *** = p < 0.001, **** = p < 0.0001). The data shown for *RAD9* strains are the same as in Figures 2 and 3 and are duplicated here for comparison to *rad9Δ*. See also Figure S4 and Table S1.

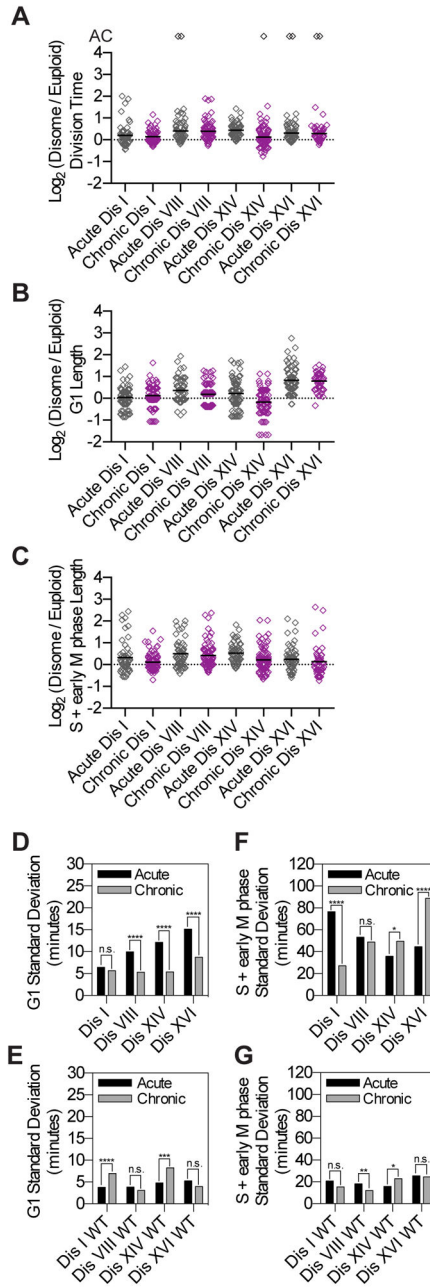


Figure 5. G1 length variability is attenuated in yeast strains harboring chronic disomies
 Chronic disomes were grown to mid-log phase in SC-D and imaged as described in Figure 2. Division time (A), G1 length (B), and S+early M phase length (C) were measured as described in Figure 2. Standard deviations for euploid (WT; E,G) and disome (Dis; D,F) populations were measured and an F-test was used to test for equality of variance between the acute and chronic populations (* = $p < 0.05$, ** = $p < 0.01$, *** = $p < 0.001$, **** = $p < 0.0001$). The data shown for acute disomes are the same as in Figure 3. However, for all strains only data from the second cell division and beyond were included in this analysis to eliminate variation due to the carbon source switch used to induce chromosome mis-

segregation in the acute disomes. Chronic disomes did not undergo a carbon source switch. See also Figure S5 and Table S1.

Author Manuscript

Author Manuscript

Author Manuscript

Author Manuscript

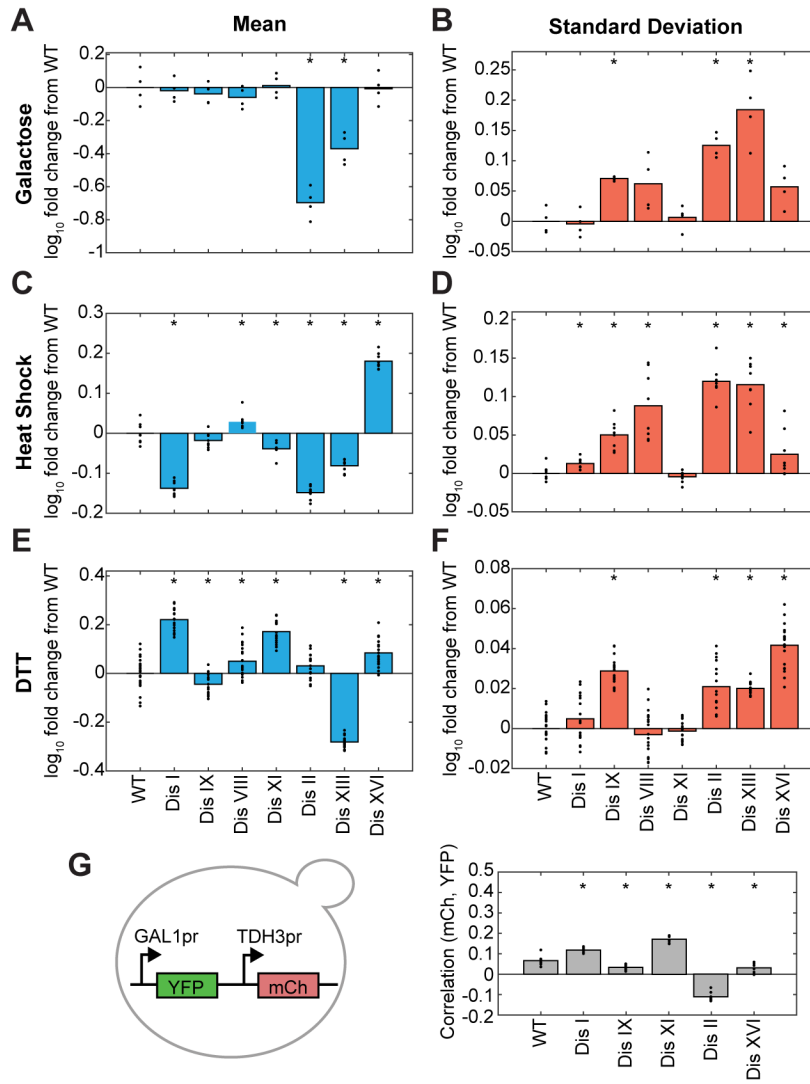


Figure 6. Cell-to-cell variability is increased in disomes in response to environmental perturbations

Mean (A,C,E) and standard deviation (B,D,F) of *GAL1pr-YFP* (A–B), *P_{4xHSE}-YFP* (C–D), and *P_{4xUPRE}-GFP* (E–F) expression at steady-state in conditions that robustly induce each reporter construct (n = 4 replicates).

(G) Correlation between *GAL1pr-YFP* and *TDH3pr-mCherry* expression in single cells (n=4 experiments). All measurements (A–G) were normalized to SSC to account for differences in cell size. Asterisks (*) in A–G indicate statistical significance between disome (Dis) and euploid (WT) populations by Wilcoxon rank sum test. See also Figures S6, S7 and Table S2.

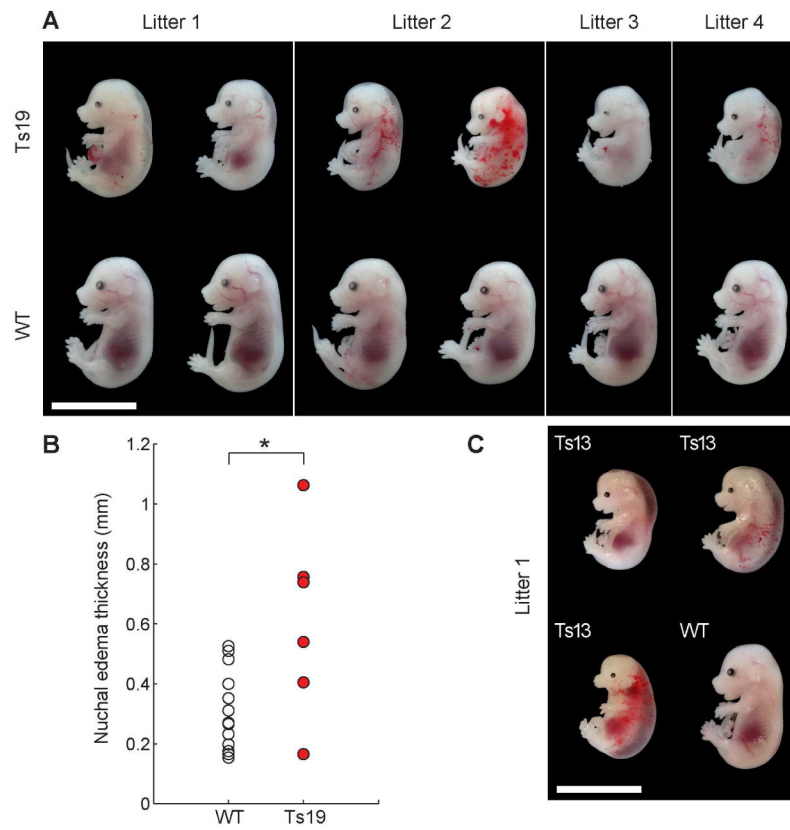


Figure 7. Non-genetic individuality in trisomic mice

(A) Trisomy 19 (Ts19) embryos and euploid (WT) littermates at gestational stage E15.5. Bar, 10 mm.

(B) Nuchal edema thickness in euploid and trisomy 19 E15.5 embryos shown in (A).

(C) Trisomy 13 (Ts13) embryos and euploid littermate at E15.5. Bar, 10 mm.